Chapter 6 Biomechanical modeling of the breast under gravity loading for preoperative tumor resection planning

Biomechanical modeling allows simulation of large deformations in breast tissues under different load conditions. Such simulations can be utilized to transform prone MRI into a different patient position, such as upright or supine. In this chapter, we present a biomechanical model of the breast to simulate the prone to supine deformation that relies on a visco-hyperelastic mechanical model and a material parameters optimization process based on the surface data alignment. The estimated tissue deformation from the preoperative to the intraoperative setting is used to determine the tumor localization for surgical planning.

6.1 Introduction

Biomechanical modeling and simulation of biological tissues have been investigated for various medical applications, such as diagnosis, clinical biopsy, preoperative planning, image-guided surgery and image registration. Recently they have been used also in the generation of synthetic data for training deep learning algorithms. Many examples of biomechanical breast models, mainly employing finite element (FE) methods for the simulation of the breast behavior, can be found in the literature: to simulate the compression of the breast between two plates, like in X-ray mammography (Samani et al. 2001; Tanner, Schnabel, et al. 2006; J. H. Hipwell et al. 2007), for 2D-3D image registration, normally simulating the compression previously mentioned (N. V. Ruiter et al. 2006; Hopp and N. V. Ruiter 2012; A. W. Lee et al. 2013; Solves-Llorens et al. 2014), for validation of 3D image registration algorithms (Schnabel et al. 2003), to simulate the deformed shape under gravity loads for surgery planning or to predict surgical outcomes (Palomar et al. 2008; Carter et al. 2008; Han, J. H. Hipwell, Eiben, et al. 2013; Eiben, Vavourakis, J. H. Hipwell, Kabus, Buelow, et al. 2016; Vavourakis et al. 2016; Danch-Wierzchowska, Borys, Bobek-Billewicz, et al. 2016; Babarenda Gamage et al. 2019; Danch-Wierzchowska, Borys, and Swierniak 2020; Xue

et al. 2021). Due to the soft nature of breast tissue, breast volume can deform significantly when the pose changes. The use of biomechanical models in the context of surgical planning or image-guided surgery allows preoperative image data to realistically deform to fit the surgical situation. This overcomes the limitations of acquiring preoperative images in a pose other than that used in surgery, such as in breast cancer surgery. Among the methods for planning breast surgery, we can distinguish between methods that use only biomechanical simulations (Palomar et al. 2008; Vavourakis et al. 2016; Babarenda Gamage et al. 2019) and those that combine them with intensity-based image registration (when a supine MRI or other supine image is available) (Carter et al. 2008; Han, J. H. Hipwell, Eiben, et al. 2013; Xue et al. 2021). It has been observed that biological soft tissues, and in particular breast tissues, exhibit a non-linear (Fung 2013), anisotropic and time-dependent mechanical response (Han, Noble, et al. 2003). A wide range of material properties for breast tissues, mostly derived from ex vivo experimental data, were used in previous studies to simulate breast tissues with linear elastic or non-linear hyperelastic models. One of the first studies was conducted by Wellman 1999 using ex vivo tissue samples. Wellman proposed an exponential stress–strain relationship for large deformations of breast tissues. Exponential constitutive models were also proposed by others authors (Krouskop et al. 1998; Azar et al. 2001). Samani et al. 2001 used a hyperelastic neo-Hookean material model to approximate Wellman's stress–strain properties. Later works have adopted hyperelastic material models in the neo-Hookean or Mooney-Rivlin form (Tanner, Schnabel, et al. 2006; Carter et al. 2008; Palomar et al. 2008; Rajagopal et al. 2008; A. Lee et al. 2010; Han, J. H. Hipwell, Eiben, et al. 2013; Mïra et al. 2018; Xue et al. 2021). All authors considered quasi-incompressible materials. The use of visco-hyperelastic models has been suggested to better describe the behavior of soft tissues subjected to large deformations (Z. A. Taylor et al. 2009). Calvo-Gallego et al. 2018 proposed to characterize the viscoelastic behavior of the human adipose tissue to simulate surgery such as breast reconstruction. The breast has usually been modeled as a heterogeneous tissue. Most of the authors considered two different tissue classes fibro-glandular and fat (Han, J. H. Hipwell, Eiben, et al. 2013; Tanner, White, et al. 2011; Samani et al. 2001; N. V. Ruiter et al. 2006). Other authors adopted a single homogeneous tissue type (Chung et al. 2008; Mertzanidou, J. Hipwell, Johnsen, Han, Eiben, Z. Taylor, Ourselin, Huisman, Mann, Bick, et al. 2014a; Del Palomar et al. 2008; Mïra et al. 2018). The experimental work of N. Ruiter, Müller, et al. 2004 found that different tissue models had no significant effect on the results. The aim of the work described in this chapter was to study the feasibility of modeling the breast behavior using a visco-hyperelastic constitutive model for simulating plausible breast deformations due to prone to supine pose change. Our simplified model will consider the breast as a homogeneous and isotropic material with sliding boundary conditions at the interface with the chest wall, without initial pre-stress conditions and with customized visco-hyperelastic

properties. The method has been evaluated using imaging data from prone and supine positions with the prerequisite that in the final scenario only the supine surface is available. The model developed provides physically realistic deformation estimations and can be used in tumor localization for surgical planning.

6.2 Materials and Methods

6.2.1 Data

For this study, we considered a subset of 15 cases of the collected dataset described in Chapter 5 Section 5.3.1. Each case consists of a prone MRI study including an MRI T2 SPAIR and a Subtraction MRI and a supine CT study. The supine CT image has been considered as reference of the surgical position for evaluation purposes. Table 6.1 reports the range and average value of a set of descriptive variables of the subset including breast volume, tumor diameter, tumor-to-skin distance, and total tumor displacement from the prone to supine position of the samples. It can be seen that large displacements occur due to the pose change and the tumor displacement ranges from 3.07 to 9.87 *cm*. The dataset covers a wide range of breast volumes to ensure the reliability of the proposed method with different breast sizes. In general, the breast size is related to deformation of the breast, and tumor position is more difficult to retrieve in the surgical position when the breast is large. Figure 6.1 shows an example of the breast pose transformation between the prone preoperative position and the supine surgical position.

	Range	**Mean**
Age [years]	46 - 82	65
Breast volume [cm^3]	812.8 - 2971.2	1663.8
Tumor diameter [mm]	4.5 - 33,6	15.0
Tumor-skin distance [mm]	5.3 - 40.3	21.6
Prone to supine tumor displacement [mm]	30.7 - 98.7	60.2

Table 6.1: Patients and Tumor Characteristics.

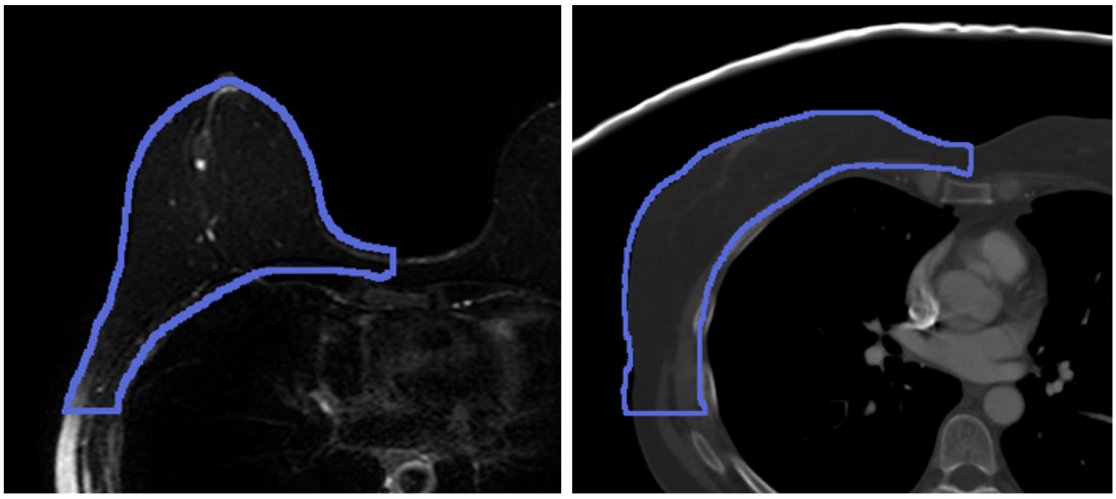

Figure 6.1: Left: prone MR image and breast contour. Right: supine CT image and breast contour.

6.2.2 FE-based Biomechanical Modeling

Patient-specific FE model of Breast

The accuracy of a breast constitutive model depends on a good understanding of the breast anatomy as well as a full characterization of the mechanical properties for each tissue. The literature have proposed models based on three or four types of tissue: adipose, glandular, skin (Schnabel et al. 2003; Del Palomar et al. 2008; Solves-Llorens et al. 2014; Xue et al. 2021) and pectoral muscle (Han, J. H. Hipwell, Eiben, et al. 2013).

In our work, we considered a simple model of the breast with only two types of tissues: the interior part of the breast volume (including fat, fibro-glandular tissue, pectoral muscle and Cooper's ligaments), which we will refer to as breast tissue, and the skin.

The breast tissue was obtained from the segmentation of the preoperative prone MRI, while the skin, that is not usually visible in the MR images, was derived directly from the outer layer of the breast segmentation. The patient-specific imaging data were segmented using Slicer 3D software (Kikinis et al. 2014) using a semi-automatic approach as described in Chapter 5 Section 5.2.1.

In addition to the behavior of breast volume, we were also interested in modeling the interface between the breast and the chest wall. To obtain the surface corresponding to the interface area, we considered the segmentation of the internal volume. This segmentation was obtained by interpolating manual segmentations of the internal area in 5 slices of the volume.

Both the prone breast and the internal volume segmentations were exported as surface

meshes and further processed in MATLAB using the *iso2mesh* library (Fang et al. 2009) to generate a more suitable mesh for the solver (reduction of the nodes density, smoothing and cleaning filters, cropping operations, etc...).

The skin was obtained as an extrusion of the outer layer of the breast volume mesh with thickness 1.5 mm.

The final prone volume surface mesh ans skin layer were automatically meshed into linear four-node tetrahedral finite elements in ABAQUS (Smith 2009), a commercial finite element software package.

Both breast tissue and skin were meshed with hybrid linear four-node tetrahedral elements (C3D4H). The hybrid formulation was chosen due to the near-incompressible nature of breast tissue, which could lead to numerical errors.

A full contact was assumed between the skin and the breast tissue. The average number of tetrahedral elements assigned to merged skin and breast tissue was $87,935$. The whole workflow from the image to the tetrahedral mesh is shown in Figure 6.2.

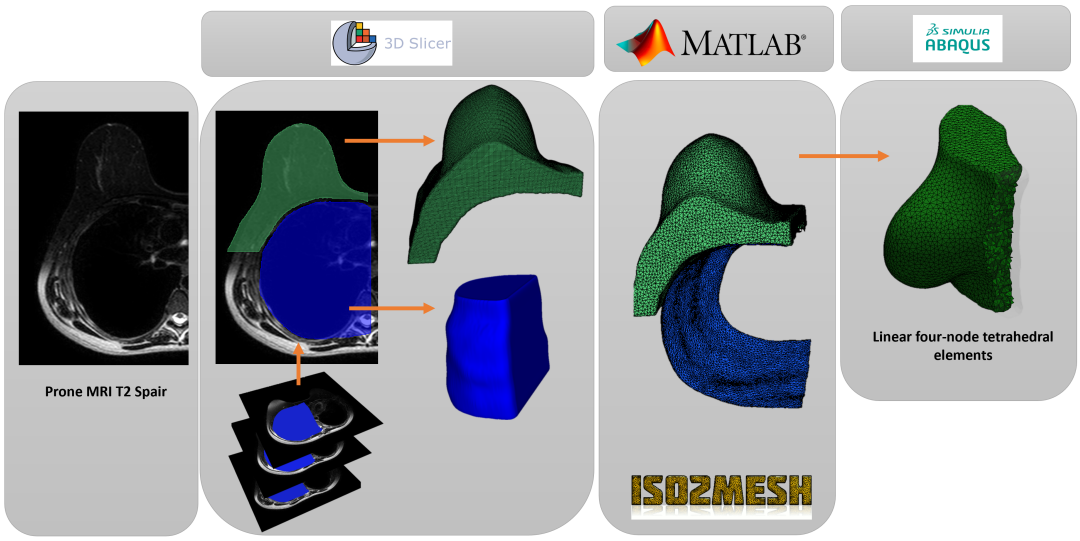

Figure 6.2: Workflow followed to obtain the tetrahedral mesh of the breast volume from the preoperative MRI.

Constitutive model of Breast tissue

Like most biological tissues, breast tissue exhibits hyperelastic characteristics under deformation. Therefore, we used a Neo-Hookean hyperelastic constitutive model to describe the stress-strain relationship of breast tissues. The neo-Hookean strain energy potential is defined as:

$$U = \frac{\mu}{2}\left(\bar{I}_1 - 3\right) + \frac{2}{K}\left(J^{el} - 1\right)^2 \tag{6.1}$$

where $\bar{I}_1$ is the first invariant of deviatoric deformation and J^{el} the determinant of the deformation gradient. μ is the initial shear modulus and K is the initial bulk modulus with $K \gg \mu$ to consider the nearly incompressible nature of breast tissue. We can write μ and K in terms of:

$$\mu = 2C_{10} \qquad K = \frac{2}{D}$$

where C_{10} is the neo-Hookean parameter; D is an incompressibility parameter.

In addition, we explored the time-varying viscoelastic properties of the breast tissue. Prony series based viscoelastic models are the most commonly used for characterizing viscoelastic properties (Wang et al. 2013). Our model of breast tissue was thus based on a Prony series based viscoelastic model. The Prony series can be written as follows:

$$C_{ij}^R(t) = C_{ij}^0\left(1 - \sum_{k=1}^{N} g_k^P\left(1 - e^{\frac{t}{\tau_k}}\right)\right), \tag{6.2}$$

where g_k^P and τ_k are the k^{th} Prony constants and the k^{th} Prony relaxation time constants, respectively; t is the current time and C_{ij}^0 is the Neo-Hookean hyperelastic parameter and N is the number of terms. Specifically, g_k^P is the k^{th} shear relaxation ratio and can be written as:

$$g_k^P = \frac{G_k}{G_0}$$

Where G_k is the k^{th} shear modulus and G_0 is the instantaneous shear modulus. Using the generalized Maxwell model for viscoelasticity, the relaxation time τ_k of each k^{th} Maxwell element can be defined as:

$$\tau_k = \frac{\eta_k}{G_k}$$

Where η_k is the dashpot constant and G_k is the spring constant of the k^{th} Maxwell element.

We only considered one term of the Prony series.

Boundary Conditions and Simulation Set Up

One of the key aspects in modeling the breast under gravity load is to realistically reproduce the breast deformation near the chest wall. Some groups assume the breast to be rigidly

fixed to the chest muscles (Samani et al. 2001; Chung et al. 2008; Hopp and N. V. Ruiter 2012; Xue et al. 2021). Other groups assume the breast to slide along the chest wall (Carter et al. 2008; A. Lee et al. 2010; Han, J. H. Hipwell, Eiben, et al. 2013; Tanner, White, et al. 2011; Mertzanidou, J. Hipwell, Johnsen, Han, Eiben, Z. Taylor, Ourselin, Huisman, Mann, Bick, et al. 2014a). We assumed the latter and modeled the sliding by defining a surface-to-surface contact. The chest wall was modeled as a rigid surface and fixed to avoid rigid displacement. The breast tissue and skin solid layer were merged to form a unique deformable body. The model only included the tumor-affected breast, thus a symmetry boundary condition was applied to simulate the junction with the contralateral breast (X-component of displacement is zero for the yellow area in Figure 6.3). Furthermore, the Z-component of displacement is zero prescribed on the superior and inferior horizontal (caudal plane) boundaries (magenta area in Figure 6.3). In this study, we neglected the effects of pre-stress and considered a simple inversion of gravity to simulate the deformation from prone to supine position, the gravity load was applied along the y direction, and the density of the breast tissue was set to 1000 kg/m^3.

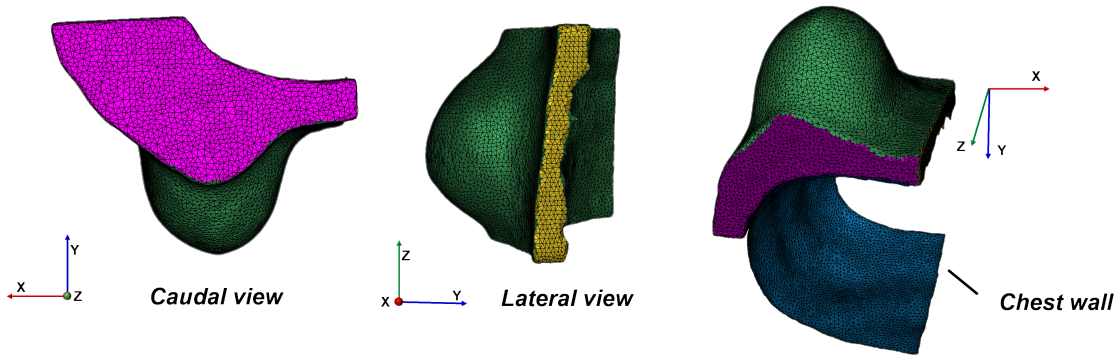

Figure 6.3: FE model of the breast and boundary conditions. Each color represents the boundary condition considered in the model: Z-component of displacement is zero prescribed on the superior and inferior horizontal (caudal plane) boundaries. X-component of displacement is zero prescribed on the the junction with the contralateral breast.

6.3 Experiments and Results

As described in Section 6.2.1 we considered 15 cases with different breast sizes and for each one we conducted several experiments with different simulation settings. The accuracy of the deformation model was assessed using different metrics described in detail in the following Section. In order to assign appropriate mechanical properties to each case, we first adjusted the parameter range and then conducted an offline optimization process for

each patient. Finally, we assessed the performance of the model for the different simulation settings.

6.3.1 Evaluation Metrics

In order to assess the accuracy of the simulations the following evaluation metrics were considered.

- **Landmarks Distance**: two landmarks were recognized in the supine CT: the position of the nipple and the centroid of the tumor. The Euclidean distance between the position of the supine landmarks in the CT and the position estimated by the simulation was calculated. Figure 6.4 shows an example of the deformed mesh outline (yellow), the landmark points marked in the CT image (green), and their estimated positions (red).

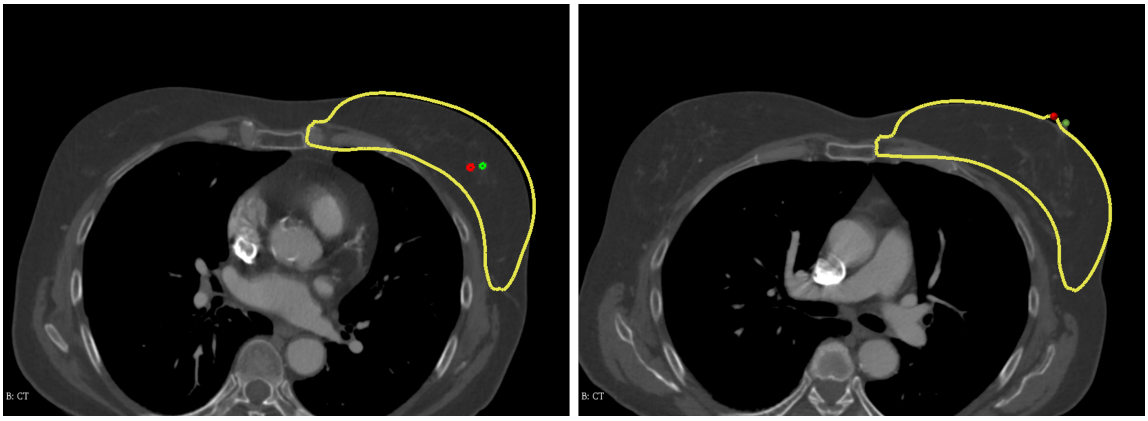

Figure 6.4: CT image and the deformed mesh outline (yellow), the landmarks points marked in the CT image (green), and their estimated positions by the biomechanical simulation (red).

- **Skin projection distance**: the distance between the skin projection of the estimated tumor centroid and the projection of the centroid of the supine tumor from the CT image. The skin projection is defined as the closest point between the center of mass of the tumor and the skin. The distance between the two projected points is a key metric to evaluate the effectiveness of the method in supporting decision making in preoperative planning and has previously been used to assess this type of algorithms Pallone et al. 2014; Duraes et al. 2019. Figure 6.5 shows a visual example of the cutaneous projections.

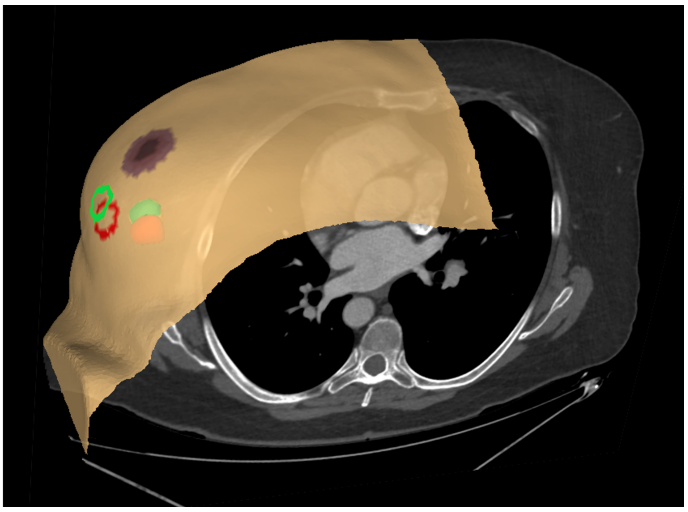

Figure 6.5: CT image and supine surface with skin projections of the estimated (red) and real (green) tumor centroid.

- **Breast volume overlap**: the volume overlap was calculated between the supine breast mask obtained using the method described in 5.2.1 and the deformed mask obtained from the deformed mesh (Figure 6.6). If we denote as S the supine mask and as D the deformed mask, the overlap was calculated using the Dice score similarity coefficient defined as follows.

$$DICE(S, D) = 2\,\frac{S \cap D}{|S| \;+\; |D|}$$

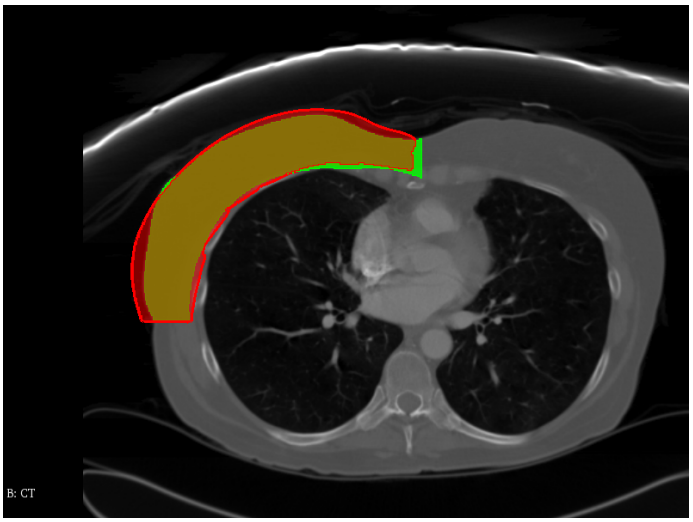

Figure 6.6: CT image, supine breast mask (green) and deformed mask (red).

6.3.2 Parameters range adjustment

To our knowledge, there are no published studies that describe the mechanical behavior of the breast as visco-hyperelastic model so we had no reference data for the viscoelastic properties of the breast. In contrast, the hyperelastic properties have been studied extensively and a wide range of shear modulus values have been reported from 160 Pa (Rajagopal et al. 2008) to 3900 Pa (Del Palomar et al. 2008). Moreover, breast mechanical properties can vary significantly depending on the patient's age, menopausal status, and overall constitution. To address this limitation our first step was to define optimal ranges for the hyperelastic μ_B and the viscoelastic g_B parameters of the breast. Furthermore, we also investigated optimal values of the friction coefficient ϕ representing the degree of sliding of the interface between the chest wall and breast tissue.

We chose a case with a medium size volume and an average age and performed multiple simulations varying μ_B, g_B and ϕ. We collected the results from 120 simulation settings varying μ_B in $[80 - 400]$ Pa, g_B in $[0.1 - 0.9]$ and ϕ in $[0.1 - 0.9]$.

The metric used to evaluate the results was the distance between the estimated nipple position and the actual nipple position marked in the CT image and the distance between the estimated tumor centroid and the supine tumor centroid segmented in the CT image.

The goal of the parameter adjustment was to find the combinations of the three parameters that ensured minimum distances between the estimated-actual nipples and tumors. As it can be seen in Figure 6.7 the best range for parameter μ_B was $[160 - 300]$ Pa, while no significant difference was found for the viscoelastic parameter g_B (Figure 6.8). For the friction coefficient, it was observed that changing ϕ almost does not impact the lateral displacements of the breast tissue when simulating the supine breast configuration (Figure 6.9). Thus we considered a value of 0.5 for ϕ. Similar results have been found in the work proposed by Mïra et al. 2018 .

The skin was modeled as a hyperelastic material (without time-varying properties) with a stiffness value proportional to the breast tissue stiffness $\mu_S = f \cdot \mu_B$ (Tanner, Schnabel, et al. 2006). The best values for f where found in the range $[4 - 10]$.

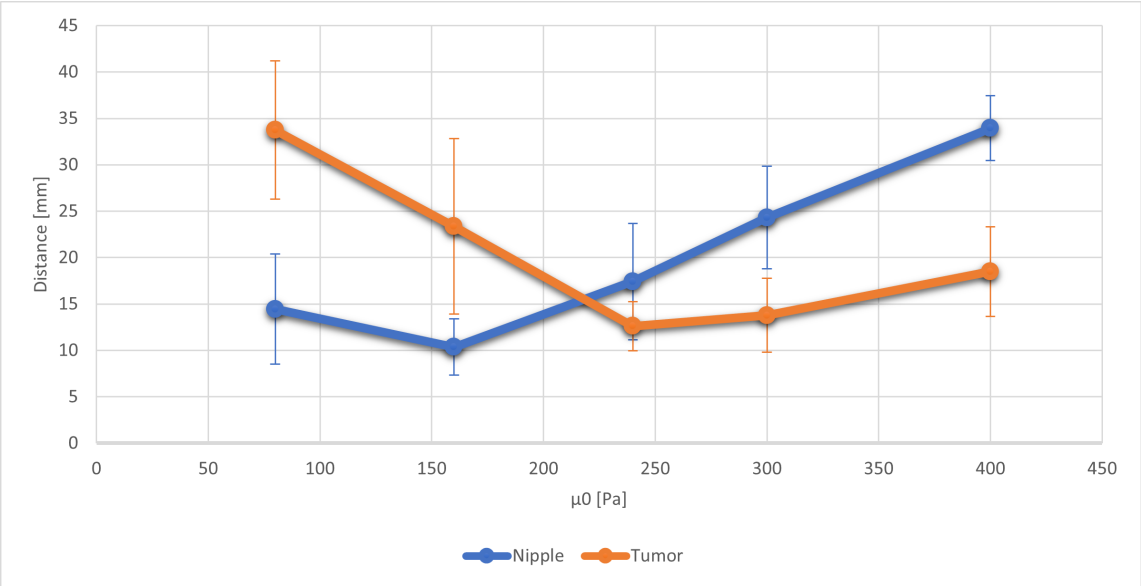

Figure 6.7: Distance values between the estimated and actual nipple point and the tumor centroid obtained by varying μ_B in the range $[80 - 400]$ Pa.

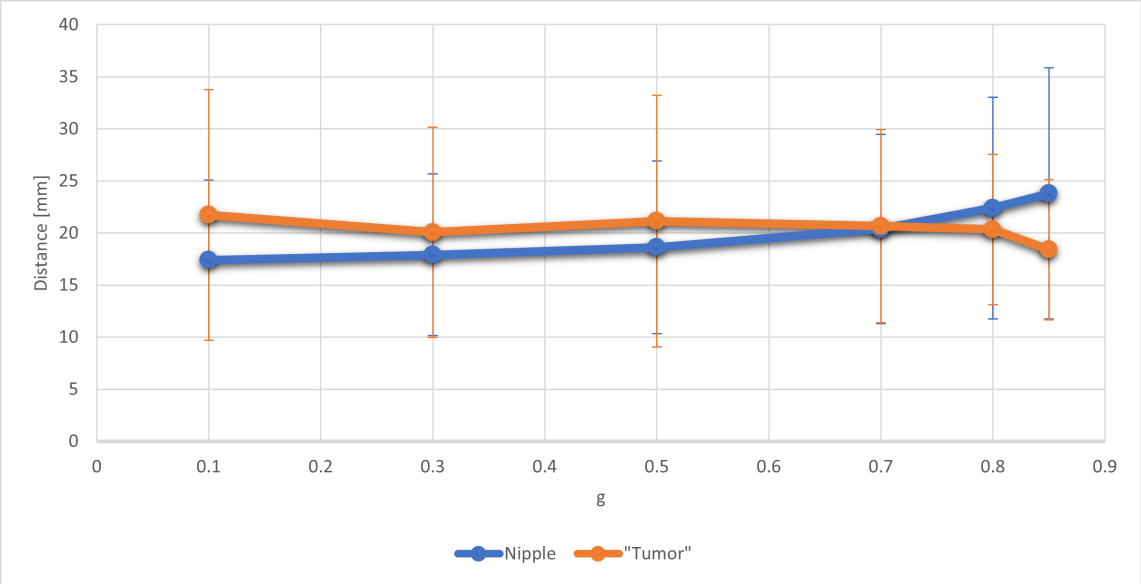

Figure 6.8: Distance values between the estimated and actual nipple point and the tumor centroid obtained by varying g_B in the range $[0.1 - 0.9]$.

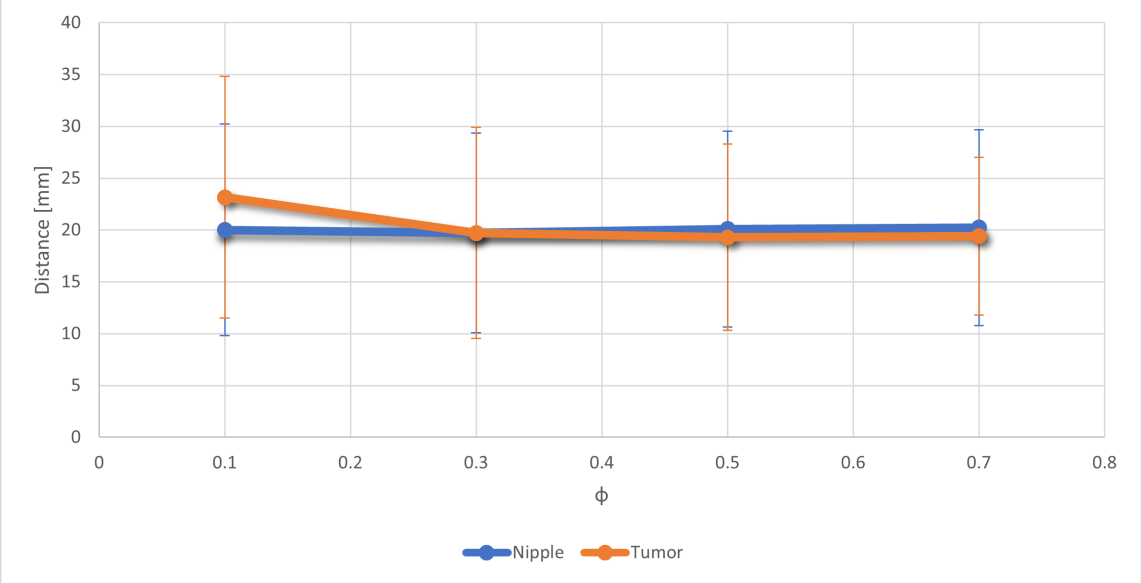

Figure 6.9: Distance values between the estimated and actual nipple point and the tumor centroid obtained by varying ϕ in the range $[0.1 - 0.9]$.

Furthermore, we also investigated the best values of g_B for three values of μ_B in the optimal range $[160 - 300]$ Pa (Figure 6.10, Figure 6.11 and Figure 6.12).

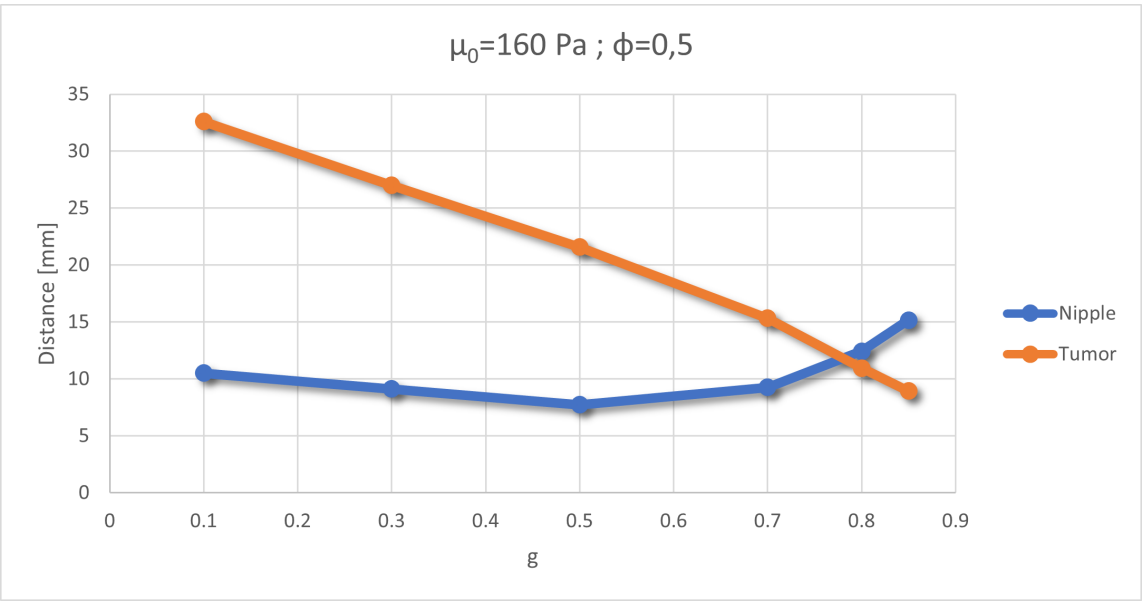

Figure 6.10: Distance values between the estimated and actual nipple point and the tumor centroid obtained by varying g_B in the range $[0.1-0.9]$ and fixing $\phi = 0.5$ and $\mu_B = 160$ Pa.

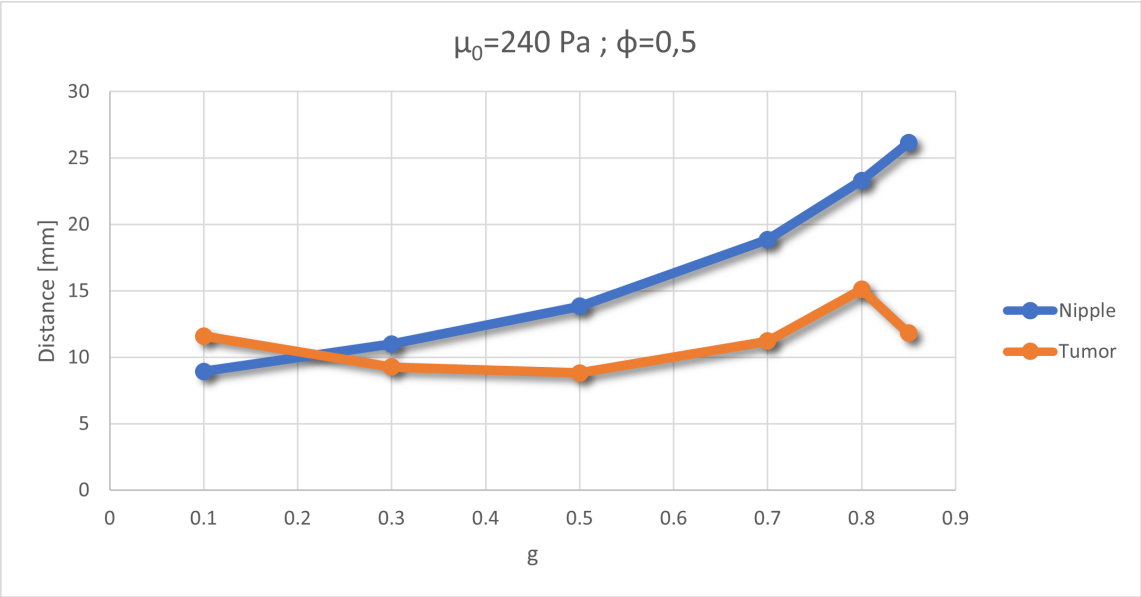

Figure 6.11: Distance values between the estimated and actual nipple point and tumor centroid obtained by varying g_B in the range $[0.1-0.9]$ and fixing $\phi = 0.5$ and $\mu_B = 240\ Pa$.

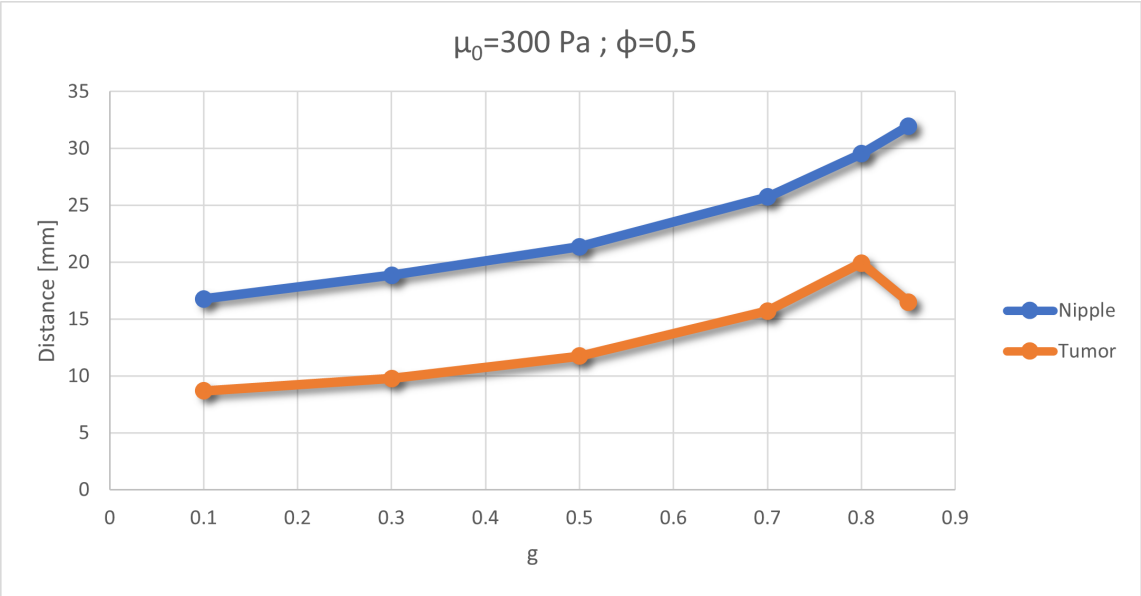

Figure 6.12: Distance values between the estimated and actual nipple point and the tumor centroid obtained by varying g_B in the range $[0.1-0.9]$ and fixing $\phi = 0.5$ and $\mu_B = 300\ Pa$.

6.3.3 Experiments

After the parameters range adjustment we selected two combinations of μ_B and g_B and for each combination three values of the skin hyperlastic parameter $\mu_S = f \cdot \mu_B$ with $f = (4, 8, 10)$. Table 6.2 reports the six combinations used for the simulations. For each case, we conducted six simulations varying the parameters according to Table 6.2. Every simulation included two parts: the breast (breast tissue and fully connected skin) and the chest wall. The same experiments were also performed without considering the sliding between the breast and the chest wall and fixing the points of the breast at the interface. Furthermore, to compare the results obtained with a standard hyperelastic breast model, we conducted the same experiments, but neglected the viscosity component.

As a first attempt to perform a patient-specific parameter optimization, the best parameterization was automatically selected for each case. The evaluation metric was the distance between the estimated position of the nipple and the actual position of the nipple in the supine position. This metric is only based on the external information and can be retrieved from the intraoperative surface acquired at the time of the surgery. For each case the combinations of parameters that ensured better nipple alignment was considered and the estimated position of the tumor was calculated and compared to the real position.

μ_B $[Pa]$	g_B	μ_S $[Pa]$	μ_B $[Pa]$	g_B	μ_S $[Pa]$
160	0.8	640	240	0.3	960
160	0.8	1280	240	0.3	1920
160	0.8	1600	240	0.3	2400

Table 6.2: Combinations of parameters μ_B, g_B and μ_S selected for the experiments.

6.3.4 Model Performance

Tables 6.3 and 6.4 report the results of the visco-hyperelastic model of the breast with sliding contact. Table 6.3 shows the final selection of parameters for each patient within the six combinations of parameters (see Table 6.2) obtained using the distance between the estimated and actual position of the nipple as an optimization metric. The average error in the nipple localization was 9.39 ± 3.96 mm, while the average tumor localization error was 9.68 ± 5.06 mm. The average distance between the skin projections of the estimated and actual tumor was 7.66 ± 6.16 mm, while the mean volume overlap was $67.77 \pm 5.30\%$.

Figures 6.13, 6.14 and 6.15 show visual examples of the results obtained with the visco-hyperelastic model with sliding.

Tables 6.5 and 6.6 report the results of the visco-hyperelastic with a fixed constraint at the interface with the chest wall. With this setup, the average error in the nipple

localization was 17.62 ± 5.65 mm, while the average tumor localization error was 15.87 ± 7.44 mm. The average distance between the skin projections of the estimated and actual tumor was 11.86 ± 9.14 mm, while the mean volume overlap was $69.71 \pm 6.16\%$. Tables 6.7 and 6.8 report the results of the hyperelastic with sliding contact. This model resulted in an average nipple localization error of 10.11 ± 6.65 mm, while the average tumor localization error was 12.83 ± 9.21 mm. The average distance between the skin projections of the estimated and actual tumor was 12.37 ± 9.99 mm, while the mean volume overlap was $66.99 \pm 5.44\%$.

case	μ_B $[Pa]$	μ_S $[Pa]$	g_B	**Nipple distance** $[mm]$
1	160	320	0.8	4.99
2	240	2400	0.3	7.84
3	240	480	0.3	10.45
4	160	1600	0.8	6.39
5	240	480	0.3	7.95
6	160	1600	0.8	9.83
7	160	640	0.8	11.35
8	160	320	0.8	9.90
9	160	1600	0.8	17.38
10	160	1600	0.8	3.89
11	160	1600	0.8	18.69
12	160	1600	0.8	10.60
13	160	1600	0.8	7.07
14	160	1600	0.8	7.04
15	240	480	0.3	7.44
mean				**9.39**
std				3.96

Table 6.3: Results of the visco-hyperelastic model of the breast with sliding contact. Selection of parameters for each patient within the six combinations of parameters (see Table 6.2) obtained using the distance between the estimated position and the actual position of the nipple as an optimization metric.

case	Tumor distance $[mm]$	Skin projection distance $[mm]$	Volume overlap [%]
1	2.97	6.55	77.7
2	2.17	5.37	70.4
3	6.83	1.22	59.7
4	21.86	24.22	65.3
5	11.94	9.26	70.0
6	14.03	5.09	70.5
7	4.28	2.63	65.2
8	12.99	14.50	63.1
9	14.73	7.52	67.8
10	5.69	0.70	70.7
11	12.74	16.37	70.0
12	6.38	1.96	58.3
13	9.94	5.98	74.4
14	9.52	5.27	61.5
15	9.18	8.23	71.9
mean	**9.68**	**7.66**	**67.77**
std	5.06	6.16	5.30

Table 6.4: Results of the visco-hyperelastic model of the breast with sliding contact in terms of tumor distance, skin projection distance and volume overlap.

case	μ_B $[Pa]$	μ_S $[Pa]$	g_B	**Nipple distance** $[mm]$
1	240	960	0.3	16.29
2	240	960	0.3	13.53
3	160	640	0.8	20.41
4	240	960	0.3	11.72
5	240	960	0.3	22.76
6	240	960	0.3	12.41
7	160	640	0.8	22.12
8	240	960	0.3	23.07
9	160	640	0.8	26.78
10	240	960	0.3	14.31
11	160	640	0.8	20.39
12	240	960	0.3	23.91
13	240	960	0.3	9.53
14	240	960	0.3	7.46
15	160	640	0.8	19.67
mean				**17.62**
std				5.65

Table 6.5: Results of the visco-hyperelastic model of the breast without sliding contact. Selection of parameters for each patient within the six combinations of parameters (see Table 6.2) obtained using the distance between the estimated position and the actual position of the nipple as an optimization metric.

case	**Tumor distance** $[mm]$	**Skin projection distance** $[mm]$	**Volume overlap** [%]
1	7.15	5.53	77.49
2	9.49	7.47	73.74
3	9.63	10.26	64.17
4	29.11	32.97	70.65
5	20.42	17.20	69.58
6	27.27	4.03	81.02
7	10.28	1.52	75.98
8	25.91	27.73	65.83
9	20.19	10.02	71.36
10	11.59	10.39	57.78
11	12.49	13.84	67.31
12	22.81	22.37	58.66
13	10.71	3.56	71.58
14	14.84	9.28	71.20
15	6.20	1.81	69.31
mean	**15.87**	**11.86**	**69.71**
std	7.44	9.14	6.16

Table 6.6: Results of the visco-hyperelastic model of the breast without sliding contact in terms of tumor distance, skin projection distance and volume overlap.

case	μ_B $[Pa]$	μ_S $[Pa]$	**Nipple distance** $[mm]$
1	160	1600	3.84
2	240	1920	7.04
3	240	960	7.52
4	240	2400	8.96
5	240	2400	28.53
6	240	2400	14.17
7	240	1920	7.80
8	160	640	1.57
9	240	2400	13.95
10	160	1600	9.47
11	240	2400	19.92
12	240	960	4.86
13	240	2400	11.10
14	240	2400	8.14
15	240	960	4.75
mean			**10.11**
std			6.65

Table 6.7: Results of the hyperelastic model of the breast with sliding contact. Selection of parameters for each patient within the six combinations of parameters (see Table 6.2) obtained using the distance between the estimated position and the actual position of the nipple as an optimization metric.

case	Tumor distance $[mm]$	Skin projection distance $[mm]$	Volume overlap [%]
1	5.02	10.34	77.07
2	8.83	7.22	69.42
3	9.20	2.85	59.81
4	29.00	31.90	64.63
5	33.96	35.69	57.00
6	4.93	5.26	69.53
7	9.53	6.79	68.64
8	3.04	6.64	63.40
9	22.64	13.56	67.95
10	8.26	10.07	69.60
11	23.34	26.48	68.53
12	7.33	7.06	60.01
13	10.61	9.84	74.46
14	7.45	3.39	62.79
15	9.29	8.54	71.97
mean	**12.83**	**12.37**	**66.99**
std	9.21	9.99	5.44

Table 6.8: Results of the hyperelastic model of the breast with sliding contact in terms of tumor distance, skin projection distance and volume overlap.

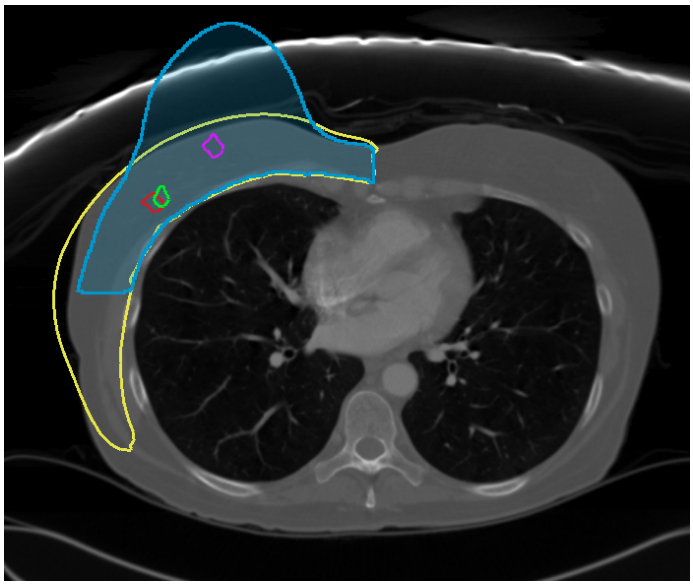

Figure 6.13: Results of the simulation for Case 1 with visco-hyperelastic model and sliding contact. The blue region is the breast volume and the magenta line is the tumor in the preoperative position. The yellow line outlines the deformed mesh, while the green and red lines represent the real and estimated tumors localizations.

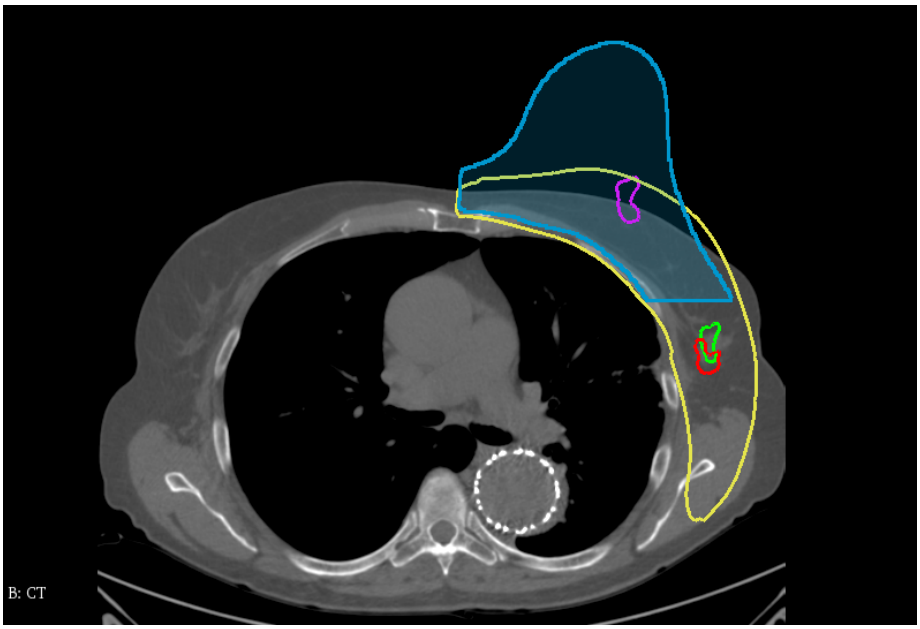

Figure 6.14: Results of simulation for Case 5 with visco-hyperelastic model and sliding contact. The blue region is the breast volume and the magenta line is the tumor in the preoperative position. The yellow line outlines the deformed mesh, while the green and red lines represent the real and estimated tumor localizations.

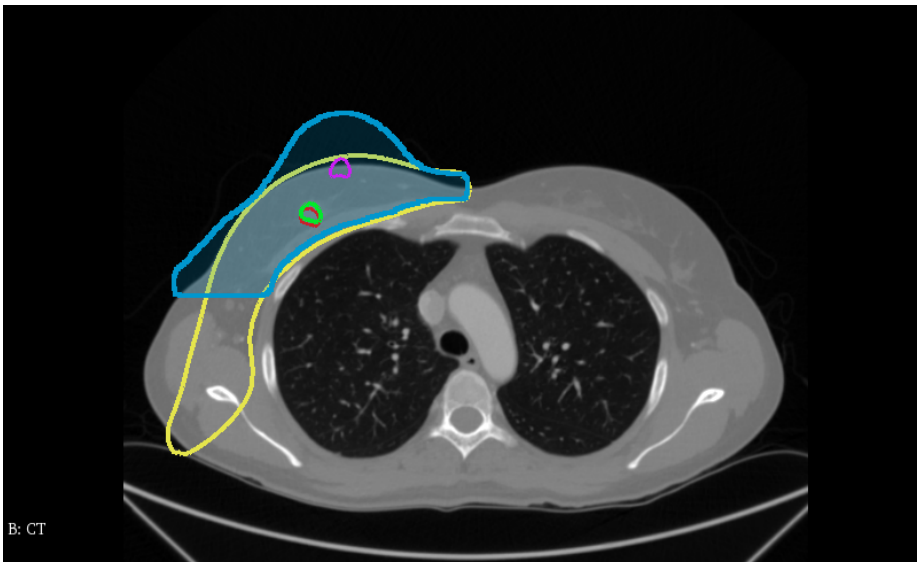

Figure 6.15: Results of simulation for Case 14 with visco-hyperelastic model and sliding contact. The blue region is the breast volume and the magenta line is the tumor both in the preoperative position. The yellow line outlines the deformed mesh, while the green and red lines represent the real and estimated tumors localizations.

6.4 Discussion and Conclusions

In this work, we propose to address the large non-rigid deformation of the breast from a supine to a prone position using a FE analysis to simulate the deformation of the breast.

We have explored the time-dependent properties of breast tissue using a visco-hyperelastic material to model and simulate the effect of gravity load using a sliding contact between the breast and the chest wall.

The variance in mechanical properties among different patients and the lack of reference data on the viscosity characterization of the breast prompted us to propose a first attempt at an optimization procedure to build patient-specific mechanical models.

We first adjusted the parameter range and then conducted an offline optimization process for each patient in a subset of parameters. The final model selected for each patient was the one that better fit the surface data information and specifically the distance between the predicted and estimated nipple.

This method could be used to support preoperative localization of breast lesions. It relies only on external data, which could be the surgical surface acquired in the operating room with an optical scan or just the location of the nipple and of some stable areas such as the sternum. In this last case, for the initial rigid alignment, it would also be necessary to acquire the positions of skin markers placed in areas with limited deformations (such as the sternum).

The geometry of patient-specific breast models were obtained from a preoperative MRI acquired in the prone position. A supine CT image has been used as reference in surgical position for the validation of the proposed method.

The average tumor localization error was 9.68 ± 5.06 mm and the average distance between the skin projections of the estimated and actual tumor was 7.66 ± 6.16 mm (see Table 6.4). The average volume overlap was 67.77 ± 5.30. This value suggests that the volume overlap is not very accurate. However, as can be seen in Figures 6.13, 6.14 and 6.15, most of the volume discrepancy occurs in the lateral posterior part. The simulated deformed tissue usually exceeds the latero-posterior limit established for the supine surface. This could be attributed to an initial mismatch between the lateral limit of the preoperative volume and the surgical surface, as this limit is difficult to establish from the MR and CT images.

Adding a viscous component to the breast provides better results in terms of absolute tumor location error and skin projection distance with respect to a hyperelastic model alone (see Table 6.8). Considering a sliding contact between the breast and the chest wall ensures more realistic deformation and better tumor localization errors (see Table 6.6).

Our method outperforms other methods of prone to supine registration that rely only on biomechanical models and surface information (average landmarks distance of 15.3 mm

(Eiben, Vavourakis, J. H. Hipwell, Kabus, Lorenz, et al. 2016); average cutaneous distance of 20.8 mm (Duraes et al. 2019)). Additionally, our results are similar to methods that use surface data to register supine-supine (average cutaneous distance of 7.2 mm (Pallone et al. 2014)). Furthermore, it has comparative results to other methods that also require an image intensity-based registration step when a supine image (MRI or CT) is available (mean (max) distance of all 9 landmarks of 8.56 mm (Han, J. H. Hipwell, Eiben, et al. 2013); mean tumor distance of 8.02 mm (Xue et al. 2021)).

The main contribution of our work is the use of a visco-hyperelastic material model to describe the behavior of the breast under gravity loading and its sliding contact with respect to a rigid chest wall. The results described in this work show that this model may allow for more accurate and realistic estimates of large deformations of breast tissue and better tumor localization errors than previously reported methods.

6.5 Limitation and Future Work

In this work, we considered only gravity as the main force responsible for the deformation of the breast from prone to supine position. However, since the breast model has been obtained from a preoperative MRI acquired under a gravity loading environment, the identification of the reference state (load-free state) could make the prediction of the final deformation more reliable.

We have considered full contact between the skin and the breast tissue; modeling the sliding between the skin and the breast could increase the accuracy of the model and make the surface data matching more reliable.

The optimization procedure has been conducted offline. Further research will consider an online optimization of the patient-specific mechanical properties using only the surface data information.

Furthermore, the results could be potentially improved using a further registration step (affine, non-rigid ICP, Bspline-based point registration, or landmark driven LDDMM) that would ensure better matching of the external surface.

One important future application of this method will be to generate ground-truth data for training deep learning algorithms. Multiple simulation of the same breast geometry in different loading conditions and varying material properties in the identified realistic ranges would allow to generate sufficient ground-truth data to learn the underline mechanical model of the breast. Such model could be used for real-time application of deformation estimations during breast surgery.

Chapter 7 Learning the prone to supine breast deformation

This chapter describes a method for learning the deformable behavior of the breast to estimate the displacement occurring from the prone position to the supine position and localize the tumor in the surgical position very efficiently.

7.1 Introduction

Traditional deformable registration techniques are based on iterative non-linear online optimization to minimize voxel-wise appearance differences and regularization terms to ensure the smoothness of displacement vector fields (DVFs). These methods usually have several disadvantages: they are expensive to calculate (time and memory), they often require multiple iterations and evaluations of energy functions and tend to stick at a local minima, especially in multimodal registration. Deep learning (DL)-based techniques based on CNN models can overcome the limitation of conventional image registration. However, while they have been widely used in medical imaging applications such as segmentation and classification for years, their use in registration has only recently become widespread (Yang et al. 2017; Dalca et al. 2018; Balakrishnan et al. 2018) due to the challenge of defining ground-truth data on which to train algorithms. Many DL-based methods have recently been published, showing remarkable results and immense potential for time-sensitive medical imaging studies, such as image-based surgery and motion tracking (Fu et al. 2020; Boveiri et al. 2020). According to the network training strategy, this type of CNN-based image registration methods can be divided into two categories: supervised DVF prediction and unsupervised DVF prediction. Figure 7.1 shows an overview of DL-based medical image registration approaches with supervised and unsurpervised DVFs prediction.

Supervised DVF prediction refers to DL models that are trained with the known ground-truth transformation between moving and fixed images. The DVF error between the predicted and reference DVFs (usually MSE) can be minimized to update the CNN model. The accuracy of the generated model depends on the quality of the ground-truth

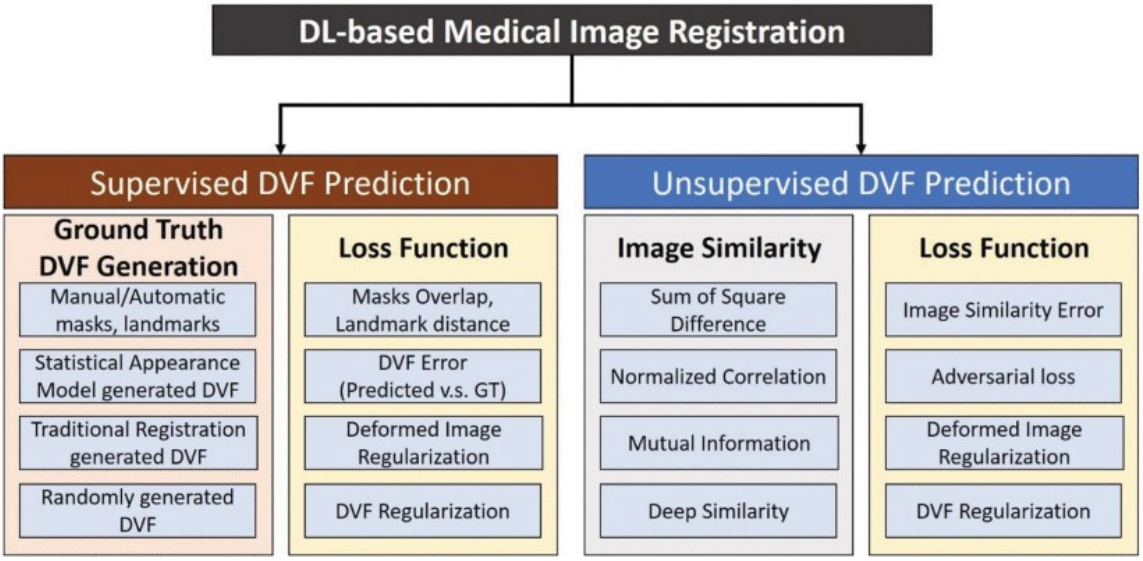

Figure 7.1: Supervised and unsupervised DVF prediction methods (Fu et al. 2020)

data used in the training process. Human experts can classify images and draw segmentation contours, but especially in 3D images, the definition of pairwise correspondence is very difficult and time consuming. To address this limitation, the ground truth DVF can be generated artificially using mathematical models or by traditional registration algorithms. Rohé et al. 2017 proposed a method to calculate reference deformations that is based on the registration of segmented regions of interest. Sokooti et al. 2019 proposed a physiological motion model to simulate ground-truth DVFs. Artificial-generated DVFs perfectly describe the deformation between pairs of images but do not always account for the noise and artifacts present between pairs of medical images, often leading to overly simplistic synthetic examples, which would not be a good representation of the deformations of real images. It is possible to mitigate this problem by using better transformation models to generate realistic transformations. In contrast, for unsupervised DVF prediction, ground-truth DVF is not needed for network training. However, robust image similarity metrics are necessary to train the network to maximize image similarity between deformed images and fixed images. In such models only the moving and fixed image pairs are provided as training data, and the model learns the deformation without the supervision of reference DVFs (unsupervised) or with supervisions other than reference DVFs (weakly supervised). The training process is supervised by loss functions similar to those used in conventional registration methods, usually comprising an image dissimilarity item and a DVF regularization term. Balakrishnan et al. 2019 proposed VoxelMorph, a framework that learns a parameterized registration function using an unsupervised convolutional neural network. It also provides a weak supervision option, in which the network is also fed with the segmentations of known corresponding structures. DL-based methods in the field of breast

cancer imaging have focused on different tasks, such as lesion classification and segmentation, image reconstruction and generation, cancer risk prediction, and prediction and evaluation of therapy response (Balkenende et al. 2022). DL-based registration techniques have also been proposed for breast imaging and used in the context of unimodal image registration with application to radiation therapy (Ouyang et al. 2020; Wodzinski et al. 2021; Fourcade et al. 2022)

In the same way that learning-based registration approaches are applied to image registration, they could also be used to solve physics-based problems involving shape registration. Real-time simulation of elastic structures is essential in many applications, such as physical-based surgical intervention. Data are generated from real-world acquisitions or can be computer generated. Once the data are processed or generated, the inputs are fed to the network and the outputs are compared to the ground truth via a loss function. CNNs are prone to be used for objects/shape registration but do require that the object is represented within a topological grid to perform convolutions. Shimada et al. 2019 proposed DispVoxNets, a pipeline for non-rigid point set registration using a 3D voxelized representation of the point sets. DispVoxNets comprises two stages, a global displacement estimation stage, and a refinement stage to remove roughness on the point-set surface. Data-driven volume-to-surface deformation estimation has been proposed in studies of analysis of intraoperative organ deformation. Such networks can learn the desired biomechanical model and predict deformations at haptic feedback rates with very good accuracy. These methods combine preoperative volume information and intraoperative partial surface information for real-time surgical guidance and navigation. Pfeiffer et al. 2020 trained a neural network on randomly generated meshes to predict displacement fields entirely on the basis of synthetic data from random organ-like meshes to estimate a displacement field within a liver from the surface of the liver. Mendizabal 2020 proposed neural networks capable of predicting the deformation of an elastic structure given variable external forces or surface deformations. They also proposed its application for real-time tracking of breast lesions in ultrasound-guided breast biopsy using a breast phantom (Mendizabal, Tagliabue, et al. 2020). The main limitations of these physics-based learning methods are related to the data generation process. The number of simulations required to train the network (several hundred simulations per boundary node) is very time consuming and when the grid resolution is increased, so does the training time. Furthermore, this approach is patient-specific and requires offline FEM-based data generation for each different geometry.

In this work, we propose a new methodology that combines DL-based image and shape registration methods to predict the large deformation of the preoperative volume of the breast given the intraoperative surface. Our method is geometry-independent and uses signed distance field (SDF) images to encode the preoperative volume and intraoperative surface. We use a fully connected network trained in a supervised manner using as ground-

truth displacement vector fields generated with a landmark driven LDDMM registration method that rely on external and internal correspondences. Moreover, different loss metrics have been proposed, one that only considers global deformation and one that also takes into account the surface and the internal structures. The method is very efficient and could be applied the intraoperative context.

The following Methods section is organized as follows. First, we describe how the prone volume and the intraoperative surface are represented to serve as input to the network. Next, we present the method for obtaining the actual deformations for training between pairs of prone volume masks and artificial supine volume masks, as well as the relevant landmark correspondences. Following, we describe the architecture used, based on a fully convolutional network adapted to the surface-volume registration task for estimating tumor location in intraoperative scenarios.

7.2 Methods

The goal of the work presented in this chapter is to estimate the displacement of the breast and the tumor when given a) the preoperative geometric model of the breast extracted from a preoperative prone image and b) the surface of the intraoperative surface as could be acquired by an intraoperative optical scan. Figure 7.2 shows a graphical scheme of the proposed method for generating ground-truth DVFs to train a network capable of recovering tumor localization when preoperative and intraoperative surfaces are given as input.

7.2.1 Voxelization

To overcome the inconsistency of the input dimensionality (different numbers of nodes between the preoperative and intraoperative meshes) we converted the points sets into a regular grid representation. Thus, the input of the network is a cube of voxels, and the output of the network becomes a displacement field with a three-dimensional displacement vector for each of these voxels. Unlike other methods that use a voxel-grid representation of the point cloud or the mesh (Shimada et al. 2019; Mendizabal, Márquez-Neila, et al. 2020) we found that encoding the preoperative and intraoperative input meshes using a voxelization in the form of distance fields on a regular grid significantly improves efficiency and convergence (Pfeiffer et al. 2020). To obtain the distance field representation of the preoperative volume V_P we calculated the distance of each point of the grid p to the closest surface point of the preoperative volume and flipped the sign of the grid points enclosed in the surface of the preoperative volume resulting in a signed distance field SDF_P (see Fig. 7.3 c and d). In the same way we obtain the distance field for the open intraoperative

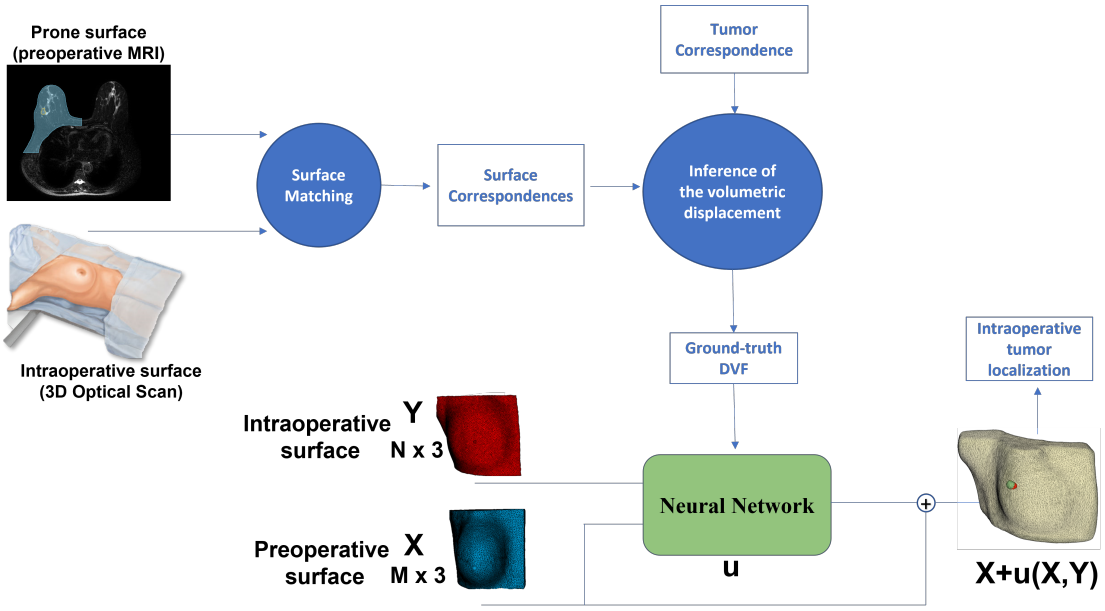

Figure 7.2: Workflow to generate ground-truth DVFs to train a network capable of retrieving tumor localization when the preoperative and intraoperative surfaces are given as input.

mesh DF_I. If we denote by $\mathbf{X}$ all points of the preoperative volume V_P and $\mathbf{Y}$ the points of the intraoperative surface S_I, the goal is to find a displacement function (a vector field) $u : \mathbb{R}^{M\times 3} \times \mathbb{R}^{N\times 3} \rightarrow \mathbb{R}^{M\times 3}$ such that $\mathbf{Y} + u(\mathbf{Y}, \mathbf{X})$ matches $\mathbf{X}$ as closely as possible. We sample the cubical volume into a grid G of $64 \times 64 \times 64$ points of interest.

7.3 Ground-truth Generation

Figure 7.4 reports the workflow for the generation of ground-truth DVFs used as reference to train the network. The generation of ground-truth is based on the matching of the prone surface, the intraoperative surface and the position of the nipple and tumor in the two positions. After the initial rigid alignment, a set of reference points correspondences is established using a surface matching procedure. Starting from these points, the axes of the breast are defined in both positions and used as fiducials to guide the prone to supine surface matching. The whole surface correspondence is obtained using a Laplacian Surface Deformation followed by an ICP algorithm. Surface and tumor points correspondences are taken as reference to drive a LDDMM registration algorithm deriving a displacement vector for each point in the preoperative breast volume. The details of the initial rigid alignment and the fiducials generation are reported in Sections 5.2.1 and 5.2.2. In the following section, we will discuss in more detail the prone to supine surface matching.

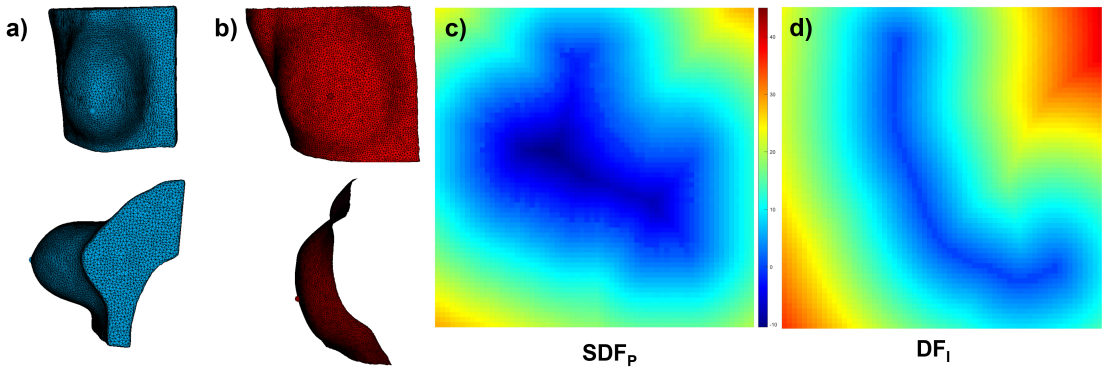

Figure 7.3: a) Preoperative volume mesh V_P. b) Intraoperative surface S_I. c) Signed distance field of preoperative volume SDF_P. d) Distance field of the intraoperative surface DF_I.

7.3.1 Prone to Supine Surface Matching

In order to obtain the transformation of the surface we use a two-step approach involving a Laplacian deformation and a non-rigid ICP algorithm (Audenaert et al. 2019) to refine the mapping and obtain a dense point-to-point matching of the two surfaces. The Laplacian deformation is a technique to deform a surface mesh that, using differential coordinates, allows the preservation of the geometric details of the surface. In contrast to the traditional global Cartesian coordinates, which can only represent the spatial location of each point, a differential surface representation carries information about the local shape of the surface, the size, and orientation of local details. Therefore, defining operations on surfaces that strive to preserve such a differential representation results in detail-preserving operations (Sorkine 2006).

Let $M = (V, E, F)$ be a given triangular mesh with n vertices. V denotes the set of vertices, E denotes the set of edges, and F denotes the set of faces. Each vertex $i \in M$ is conventionally represented using absolute Cartesian coordinates, denoted by $v_i = (x_i, y_i, z_i)$. The Laplacian representation of a vertex in a surface mesh is one way to encode the local neighborhood of a vertex in the surface mesh. In this representation, a vertex v_i is associated with a 3D vector δ_i defined as the difference between the absolute coordinates of the vertex v_i and the center of mass of its immediate neighbors in the mesh:

$$\delta_i = v_i - \frac{1}{d_i} \sum_{j \in N(i)} v_j$$

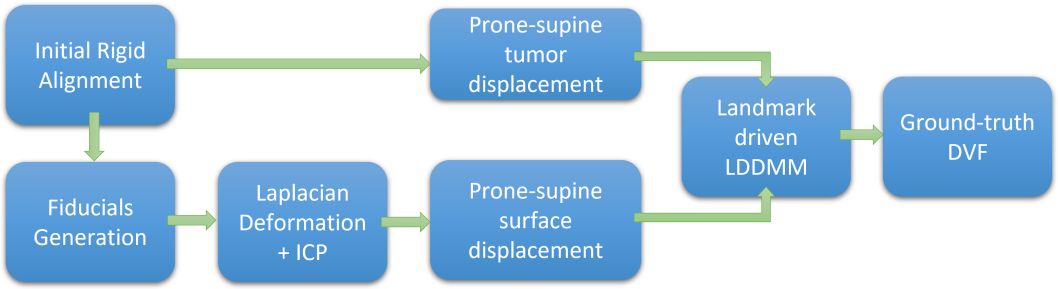

Figure 7.4: Workflow for the generation of ground-truth DVFs used as reference to train the network.

where $N(i) = \{j \mid (i,j) \in E\}$, the set of vertices adjacent to v_i and $d_i = |N(i)|$ is the number of immediate neighbors of i (the degree or valence of i). To add geometric weighting possibilities, one can extend equation 2.2 by adding weights as:

$$\delta_i = \frac{1}{\sum w_{ij}} \sum_{j \in N(i)} w_{ij} \left(v_i - v_j\right)$$

where w_{ij} is the weight of the edge (i,j).

Considering a surface mesh with n vertices, let L be the Laplacian matrix of the mesh and V a $n \times 3$ matrix containing the Cartesian coordinates of the vertices. It is possible to define its Laplacian representation in matrix form as Δ a $n \times 3$ matrix:

$$\mathrm{LV} = \Delta$$

The mesh deformation is achieved defining: a) a subset of k vertices referred to as the control vertices; b) the final position for each control vertex (deformation constraints); c) a weighting scheme for the Laplacian matrix. The deformation process must follow the deformation constraints while preserving the Laplacian representation as much as possible. The final surface is achieved by solving the following system of equations:

$$\begin{bmatrix} \mathbf{L}_\mathrm{f} \\ \mathbf{0} \quad \mathbf{I_c} \end{bmatrix} \mathrm{V_d} = \begin{bmatrix} \Delta_\mathbf{f} \\ \mathrm{V_c} \end{bmatrix}$$

$\mathbf{V}_\mathrm{d}$ is the matrix containing the coordinates after deformation. The last k rows of the system correspond to the control vertices. $\mathbf{L}_\mathrm{f}$ denotes the Laplacian matrix of the unconstrained vertices, whose elements are calculated using a cotangent weight scheme.

Given an edge of the surface mesh, its corresponding cotangent weight is the mean of the cotangents of the angles opposite to the edge. $\mathbf{I_c}$ is the $k \times k$ identity matrix, $\Delta_\mathbf{f}$ denotes the Laplacian representation of the unconstrained vertices, removing the rows corresponding to the control vertices. V_c is the matrix that contains the final position of the control vertices.

We chose as control vertices the breast axes computed for both positions as described in Section 5.2.2, and we fix the points belonging to the internal boundary of the breast volume (Figure 7.5 a, b, c). A typical deformed mesh is shown in Figure 7.5 d.

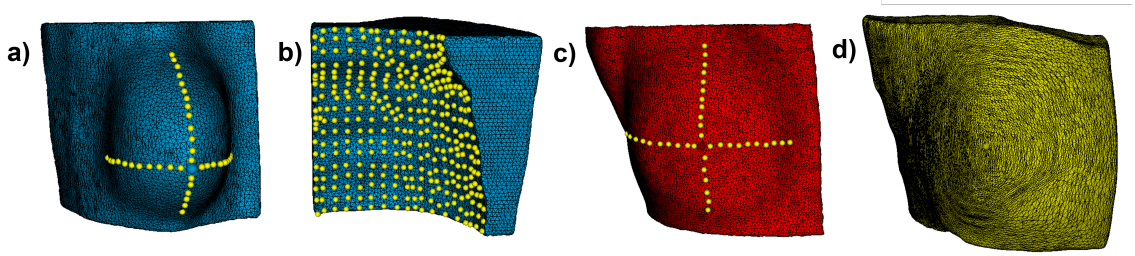

Figure 7.5: a) Prone breast volume mesh and fiducial points of the breast axes (yellow). b) View of the back side of the prone breast volume mesh and internal boundary points (yellow) considered fixed during the Laplacian deformation. c) Prone surface and corresponding breast axes fiducial points (yellow). d) Estimated deformed mesh after the Laplacian Deformation and ICP algorithm.

7.3.2 Inference of the Internal Displacement Field

After the surface matching procedure, we obtain the displacement vectors defined at all the surface points. These surface points correspondences and the prone-supine tumor correspondence are the landmarks that guide the subsequent LDDMM algorithm to build a ground-truth displacement field. To generate a DVF defined in all points of the grid, we use a landmark driven LDDMM algorithm that computes the displacement field minimizing the distance between the landmarks, but also ensuring volume preservation, smoothness of DVFs, and consistency. As mentioned in Section 5.2.3, the LDDMM framework calculates an optimal transformation between the prone volume mask I_P and the supine volume mask I_S image, integrating the vector field that is found by minimizing the equation 5.1. In this case, in the spring term E_S (Eq. 5.1) we do not consider a uniform weight vector (w), but assign a greater weight to the nipple and to the tumor centroid to force the matching of these markers as their location is known.

To obtain a reliable ground-truth DVF for each pair (I_P , I_S) we have optimized the parameters of the LDDMM algorithm until the LDDMM-estimated positions of the nipple

and tumor centroid satisfied a predefined distance requirement ($< 3.5\ mm$ for the tumor centroid and $< 6\ mm$ for the nipple). Figure 7.6 shows the workflow of the optimization process used for the generation of ground-truth DVF. A typical generated DVF is shown is Figure 7.7. Additionally, we interpolate the ground-truth displacement field $U_G T$ into the same grid and set the displacement values of the points outside the preoperative volume to $(0, 0, 0)$.

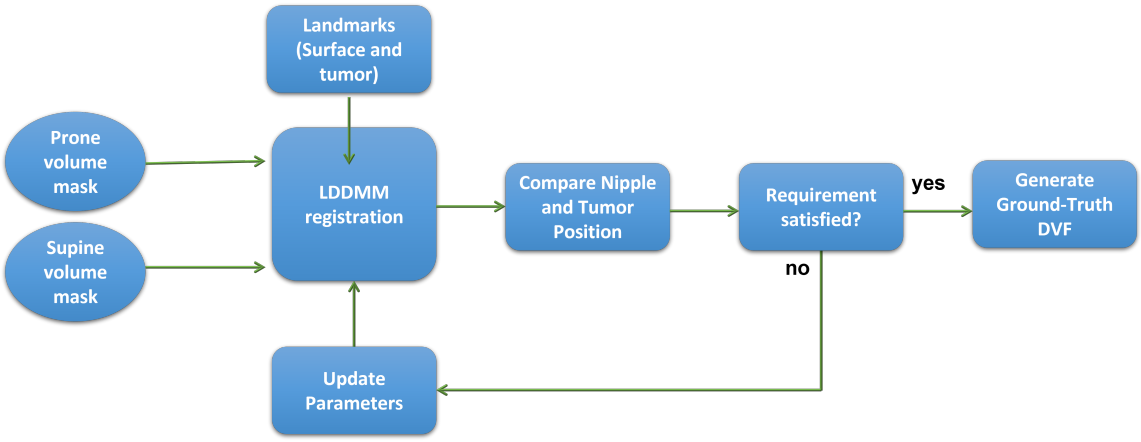

Figure 7.6: Optimization process for ground-truth DVF generation. LDDMM-estimated nipple and tumor positions were compared to the real positions. LDDMM parameters were updated until the distance was less than a predefined tolerance value.

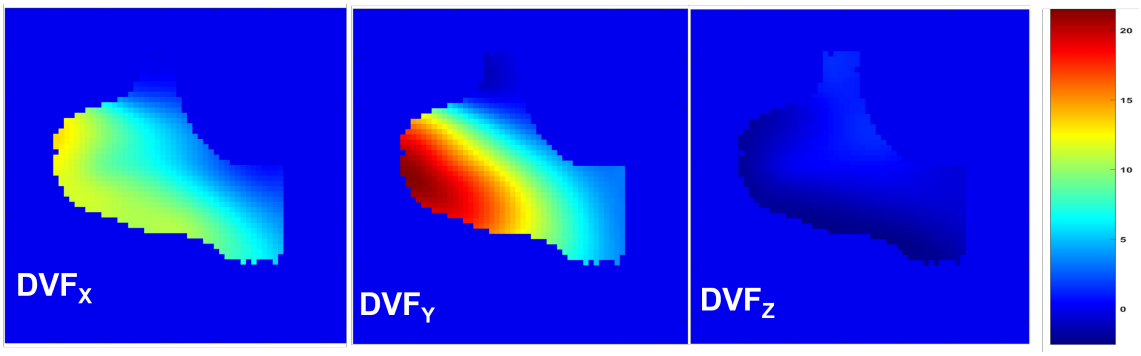

Figure 7.7: Typical ground-truth DVF generated by the proposed workflow.

7.4 Network Architecture and Training

To estimate the displacement field U_{EST}, the network is given the full preoperative prone volume SDF_P and the intraoperative surface DF_I. Before passing the data to the network, we normalize SDF_P, DF_I, and U_{GT} to improve the convergence properties. Formally, we want the network to estimate the function:

$$F(SDF_P, DF_I) = U_{EST}$$

We use D_{vn} as base architecture we used the one proposed by Shimada et al. 2019, a fully convolutional architecture with 3D convolutions similar to the U-Net (Ronneberger et al. 2015). Such architectures present an encoder-decoder structure and skip connections to allow for an abstract low-resolution representation while preserving high-resolution details. The precise architecture is shown in Table 7.1. Unlike the original U-Net, this network works with three-dimensional input data, and all convolutions are calculated across the three dimensions. All convolutions have a kernel side length of 3 and padding of 1, and each is followed by a LeakyReLU activation function.

The displacement field output from the network U_{EST} is compared to the displacement field of the ground-truth U_{GT} using the mean absolute error. Given a grid G of $N \times N \times N$, the loss function L_{MSE} is written as follows:

$$L_{MSE} = \frac{1}{N^3} \sum_{p} M(p) \parallel U_{EST}(p) - U_{GT}(p) \parallel$$

where N^3 is the number of points of the grid, $M(p)$ is a masking function that is zero if p is outside the prone breast volume and one otherwise and $\parallel \bullet \parallel$ denotes the magnitude of a vector.

We also designed another loss function L_{ST} by adding to L two other terms L_T and L_S.

$$L_{ST} = L_{MSE} + L_S + L_T$$

If we denote by p_{PS} the N_{PS} points of the preoperative surface S and by p_I the points of the intraoperative surface, L_S is defined as the mean of the smallest distances of every preoperative surface point p_{PS} to any intraoperative points p_I.

$$L_S = \frac{1}{N_{PS}} \sum_{p_{PS} \in S} \{\min_{p_I \in I} \{d(p_{PS}, p_I)\}\}$$

L_T is defined in the same way, but considering the distance between the N_{TP} points p_{TP} of the preoperative tumor T_P and the points p_{TI} of the intraoperative tumor T_I.

$$L_T = \frac{1}{N_{TP}} \sum_{p_{TP} \in T_P} \{\min_{p_{TI} \in T_I} \{d(p_{TP}, p_{TI})\}\}$$

Adding these terms to the computation of the loss allows to specifically penalize the distance between the deformed preoperative and intraoperative surfaces, and the distance between the estimated and real tumor.

We trained the network with Adam optimizer (Kingma et al. 2014) with a learning rate of $3 \cdot 10^{-4}$. Furthermore, we used a 5-fold cross-validation with 1500 epochs, and selected the model with the best convergence of the mean registration error.

ID	Layer	Output Size	Kernel	Padding/Stride	Concatenation
1	Input	$64 \times 64 \times 64 \times 2$	–	–	–
2	3D Convolution	$64 \times 64 \times 64 \times 8$	$7 \times 7 \times 7$	3/1	–
3	LeakyReLU	$64 \times 64 \times 64 \times 8$	–	–	–
4	MaxPooling 3D	$32 \times 32 \times 32 \times 8$	$2 \times 2 \times 2$	0/2	–
5	3D Convolution	$32 \times 32 \times 32 \times 16$	$5 \times 5 \times 5$	2/1	–
6	LeakyReLU	$32 \times 32 \times 32 \times 16$	–	–	–
7	MaxPooling 3D	$16 \times 16 \times 16 \times 16$	$2 \times 2 \times 2$	0/2	–
8	3D Convolution	$16 \times 16 \times 16 \times 32$	$3 \times 3 \times 3$	1/1	–
9	LeakyReLU	$16 \times 16 \times 16 \times 32$	–	–	–
10	MaxPooling 3D	$8 \times 8 \times 8 \times 32$	$2 \times 2 \times 2$	0/2	–
11	3D Convolution	$8 \times 8 \times 8 \times 64$	$3 \times 3 \times 3$	1/1	–
12	LeakyReLU	$8 \times 8 \times 8 \times 64$	–	–	–
13	3D Deconvolution	$16 \times 16 \times 16 \times 64$	$2 \times 2 \times 2$	0/2	12&10
14	3D Deconvolution	$16 \times 16 \times 16 \times 64$	$3 \times 3 \times 3$	1/1	–
15	LeakyReLU	$16 \times 16 \times 16 \times 64$	–	–	–
16	3D Deconvolution	$32 \times 32 \times 32 \times 32$	$2 \times 2 \times 2$	0/2	15&7
17	3D Deconvolution	$32 \times 32 \times 32 \times 32$	$5 \times 5 \times 5$	2/1	–
18	LeakyReLU	$32 \times 32 \times 32 \times 32$	–	–	–
19	3D Deconvolution	$64 \times 64 \times 64 \times 16$	$2 \times 2 \times 2$	0/2	18&4
20	3D Deconvolution	$64 \times 64 \times 64 \times 16$	$7 \times 7 \times 7$	3/1	–
21	LeakyReLU	$64 \times 64 \times 64 \times 16$	–	–	–
22	3D Deconvolution	$64 \times 64 \times 64 \times 3$	$3 \times 3 \times 3$	1/1	–

Table 7.1: U-Net style architecture of DispVoxNets (Shimada et al. 2019).

7.5 Experiments and Preliminary Results

7.5.1 Data

As detailed in Section 5.3.1 the dataset consists of 67 retrospective cases of breast cancer. Each case included a preoperative T2 SPAIR MRI and a CT image in the supine position used to simulate the intraoperative surface and to locate the tumor in the supine position for evaluation. The number of cases was increased considering both the breast affected by the tumor and the contralateral breast, which can vary in shape and constitution, leading to different deformations. We also included two additional cases (both breasts) that were excluded because the lesion was not clearly visible on the CT image. Therefore, the final number of breasts in the dataset was 138. Each case was pre-processed as described in Section 5.2.1. We used 118 breasts for training and the remaining for testing, ensuring an

equal distribution of breast sizes between the two sets. In addition, we ensured that the split assigns complete cases (tumor-affected breast and corresponding controlateral breast) to training or to testing sets. As a result, only half of the test samples were tumor-affected breasts and were used to estimate tumor-related evaluation metrics. Training samples were subjected to the ground-truth DVF generation process described in Section 7.3.2. In the case of the contralateral breasts, for which no internal marker is available to generate the reference DVFs, we used only the surface and nipple correspondences.

7.5.2 Experiments and Evaluation

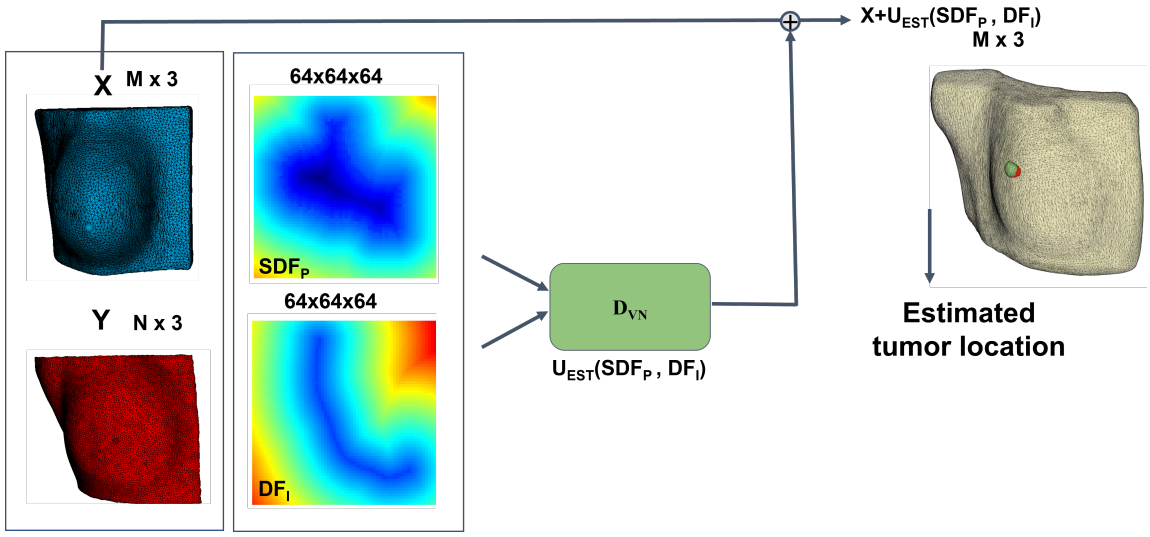

Figure 7.8: Given a preoperative volume and a intraoperative surface, the distance fields image were calculated and presented as inputs to the network D_{vn}. The estimated displacement U_{EST} was used to calculate the estimated supine volume mesh of the breast and the estimated position of the tumor.

We performed experiments with two network models of D_{vn}, one trained with the loss function L_{MSE} and one with the loss L_{ST}. The same split was adopted in both experiments.

The network was implemented using PyTorch (Paszke et al. 2019), and built in a PC with a GPU NVIDIA GeForce GTX 1080 8GB and NVIDIA Quadro P6000 24GB.

We evaluated the registration accuracy of our method using the metrics described in Section 6.3.1: the distance between the estimated and actual tumor centroid, the distance between the skin projections of the estimated and actual tumor centroid, and the Dice score that was calculated as the overlap between the estimated supine volume mesh and the artificial supine volume calculated as described in Section 5.2.1. For this purpose, first the distance fields for the preoperative volume V_P and the intraoperative surface S_I,

were calculated for the validation samples and then the network D_{vn} was used to estimate the displacement of the breast volume (see Figure 7.8). The process of estimating the displacement field takes roughly 130 ms. The estimated displacement field U_{EST} was used to calculate the estimated supine volume mesh of the breast and the estimated position of the tumor.

7.5.3 Results

We compared the results obtained with two models D_{vn}, one trained using as loss function L_{MSE} and one D_{vn} trained using as loss function $L_{ST} = L_{MSE} + L_S + L_T$ that specifically penalizes the distance between the deformed preoperative surface and the intraoperative surface, and the distance between the estimated and real tumor. Table 7.2 reports the results obtained with the two models. The average tumor distance was 17.40 ± 6.10 mm, while the average projection distance of the skin was 14.71 ± 6.21 mm and the dice score was $80 \pm 3\%$ for the model D_{vn} - L_{MSE}. Better results were achieved using the D_{vn} - L_{ST} model with an average tumor distance of 15.46 ± 3.96 mm and an average skin projection distance of 13.38 ± 4.61 mm. The dice score was slightly lower with a value of $78 \pm 4\%$. Qualitative results obtained applying the D_{vn} - L_{ST} model are shown in Figure 7.9.

Model	**Tumor Distance [mm]**	**Skin projection Distance [mm]**	**Dice Score [%]**
D_{vn} - L_{MSE}	17.40 ± 6.10	14.71 ± 6.21	80 ± 3
D_{vn} - L_{ST}	15.46 ± 3.96	13.38 ± 4.61	78 ± 4

Table 7.2: Results obtained with two models D_{vn}, one trained using as loss function L_{MSE} and one D_{vn} trained using as loss function $L_{ST} = L_{MSE} + L_S + L_T$.

7.6 Conclusion and Discussion

In this work, we have designed a new methodology based on a deep neural network to efficiently derive the large deformations that occur between the volume of the breast extracted from a preoperative prone MRI and the intraoperative supine surface to estimate the tumor displacement for planning surgery in breast cancer treatment. We adapted the architecture proposed by Shimada et al. 2019, designed for point-sets alignment and trained with thousand of meshes with known ground-truth displacement vectors, to be used for a surface to volume registration. Furthermore, we adopted a distance field representation of the inputs that was more efficient and allowed faster training and prediction.

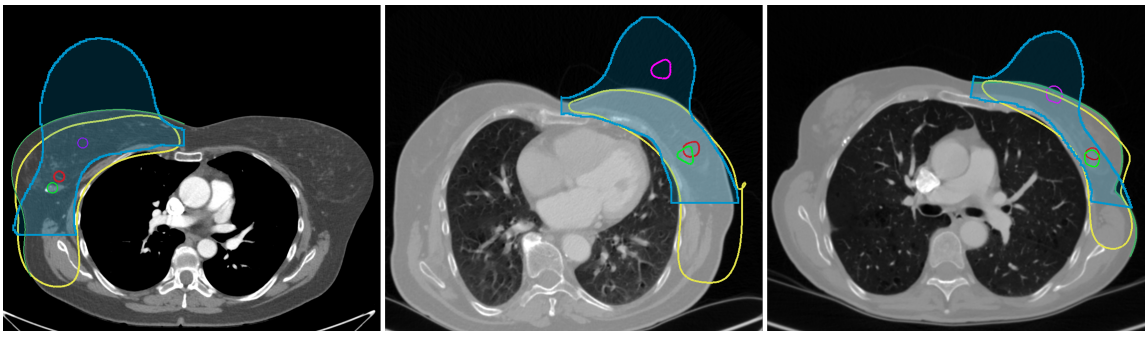

Figure 7.9: Result of registration with the D_{vn} - L_{ST} model. The blue region is the preoperative breast volume and the magenta line is the preoperative tumor. The yellow line outlines the estimated deformed mesh, while the green and red lines represent the actual and estimated tumors.

The network is trained in a supervised manner using as ground-truth displacement vector fields generated with a landmark driven LDDMM registration method that rely on external and internal correspondences. Furthermore, different loss metrics have been proposed, one that only considers global deformation (MSE of the estimated and ground-truth DVFs (D_{vn} - L_{MSE})) and one that also takes into account the surface and the internal structures (distance between the deformed preoperative and intraoperative surface and the estimated and actual tumor location (D_{vn} - L_{ST})).

The method was evaluated in 10 real clinical cases. Better results were obtained using the D_{vn} - L_{ST} model with an average tumor localization error of 15.46 ± 3.96 and an average surface projection distance of 13.38 ± 4.61.

The model performance is comparable to the landmark driven registration proposed in chapter 5. Given a preoperative volume and an intraoperative surface encoded in a distance field image, the prediction of the displacement field takes approximately 130 ms. Due to the high speed, this method could also be used in other real-time applications in surgery or radiation therapy. Furthermore, it could be used as an initial fast alignment before proceeding to other registration techniques. The network can be easily used with other breast geometries that have not been seen during training, in contrast to other proposals that need a new training for every new geometry (Mendizabal, Márquez-Neila, et al. 2020). Furthermore, our method has been tested in 10 clinical cases, unlike other similar proposals ((Pfeiffer et al. 2020) performed registration only for two patients during surgery).

The validation of the current proposal was developed using, instead of the intraoperative surface, the patient's surface from a supine CT image, which is close to the surgical position.

To ensure that the method can be easily used in the surgical setting, the proposed workflow has been designed to use the intraoperative breast surface acquired by an optical scanner in the operating room, minimally altering the surgical procedure.

7.7 Limitation and Future Work

The major limitation of our work is the limited amount of data. Furthermore, the training process is based on ground-truth DVFs that are generated using a landmark driven LDDMM with a very limited number of internal markers. Identifying more internal markers in addition to the tumor centroid could lead to a more realistic inference of internal displacement of the breast tissue and increase the reliability of the generated DVFs.

Further research will also consider the use of biomechanical simulations to significantly increase the training data, and to generate a learning model compatible with the biomechanical behavior ensuring more realistic and accurate reference DVFs.

Chapter 8 Concluding remarks

8.1 Discussion and Conclusion

In the context of breast cancer management, an accurate diagnosis and delineation of the extent of breast cancer can be achieved using preoperative MRI acquisitions in the prone position. However, large deformations occur between the preoperative (prone) position and the surgery that is typically performed in the supine position. Therefore, breast lesions undergo significant displacement between the preoperative image and the intraoperative position and require preoperative localization. Currently, wire-guided localization (WGL) is the most widely used method for locating non-palpable breast lesions (Chan et al. 2015). The limitations of WGL include technical complications such as wire transection and migration, patient discomfort, and poor cosmetic outcome (Azoury et al. 2009; Volders et al. 2016; Kiruparan et al. 2021).

The main objective of this thesis was the development of techniques to provide alternatives or complementary tools for preoperative tumor localization in the treatment of breast cancer.

All the methods developed in the work were designed to require only the surface of the patient in the surgical position and a standard of care diagnostic preoperative prone MRI in which the tumor is clearly visible. However, the work has been developed using the surface of the patient from a supine CT image. Furthermore, the tumor identified in the supine image has been used to validate the developed techniques.

The main challenge of the work has been to predict the internal displacement of the breast and the location of the tumor in the surgical position by matching only the exterior based on the surface data.

We have followed two main approaches to obtain the tumor localization in the surgical position: 1) using image registration techniques adapted to perform surface driven registration 2) biomechanical modeling of the breast under the gravity load using surface information to optimize the material properties.

The first approach, described in chapter 5, propose a novel method for performing a surface driven registration of a preoperative prone volume to the surgical position with-

out any intensity information. We have designed a framework that, after an initial rigid alignment, generates an artificial volume in the intraoperative position and automatically defines surface fiducials points based on the position of the nipple (the only available and reliable skin marker). The generated supine volume and fiducials set is used for the subsequent landmark driven LDDMM registration used to estimate the prone to supine volumetric deformation and estimate the localization of the tumor in the surgical position. The method was evaluated in 67 clinical cases with an average localization error of 16.21 $\pm$ 8.18 mm and an average distance between the cutaneous projections of the actual and estimated tumor of 13.86 ± 7.59mm. This preoperative localization approach could be useful to guide the surgeon towards the location of the tumor without the limitations of WGL. The benefit of use could be of interest even in combination with other guidance mechanisms such as the wire itself, radar guidance, radiofrequency identification or radioactive seeds (M. K. Lee et al. 2020; Tingen et al. 2020). The tumor target error results obtained are very competitive considering that they are obtained without including biomechanical models in the registration workflow nor the requirement of acquiring supine MRI or other preoperative supine imaging. Some prior hybrid methods using supine image information achieve better results. However, they have been tested in a very reduced datasets (less than 5 cases) without ensuring generalization of the proposed technique (Carter et al. 2008; A. Lee et al. 2010, Han et al. 2013, Eiben et al. 2013). The use of surgical surface information combined with biomechanical models produced similar results (average landmarks distance of 15.3 mm) (Eiben et al. 2016) or worse results (average cutaneous distance of 20.8 mm) (Duraes et al. 2019). Recent research using a hybrid approach and combining biomechanical models and supine surface information has obtained very competitive results (average tumor distance of 8.05 mm), although the dataset is still limited in number (25 cases) and with a smaller percentage of medium and large breast volume cases (Xue et al. 2021).

The second approach, described in Chapter 6, proposes a biomechanical model of the breast under gravity load to simulate the prone to supine deformation. The breast has been modeled as a visco-hyperelastic material and a patient-specific optimization process based on the alignment of the surface data has been performed. The estimated tissue deformation from the preoperative to the intraoperative setting is used to determine tumor location. This method was evaluated in 15 clinical cases with an average tumor localization error of 9.68 ± 5.06 mm and average distance between the cutaneous projections of the actual and estimated tumor of 7.66 ± 6.16 mm. Furthermore, we found that adding a viscous component to the breast provides better results in terms of absolute tumor location error and skin projection distance with respect to a hyperelastic model alone. Our method outperforms other methods of prone to supine registration that rely only on biomechanical models and surface information (average landmark distance of 15.3 mm (Eiben et al. 2016); average cutaneous distance of 20.8 mm (Duraes et al. 2019)). Additionally, our results are

similar to methods that use surface data to register supine-supine (average cutaneous distance of 7.2 mm (Pallone et al. 2014)). Furthermore, it has comparative results to other methods that also require an image intensity-based registration step when a supine image (MRI or CT) is available (mean distance (max) of the 9 landmarks of 8.56 mm (Han et al. 2013); mean tumor distance of 8.02 mm (Xue et al. 2021)).

From the first approach, we also derived a secondary branch, described in chapter 7, which relies on ground-truth DVFs generated with the landmark driven LDDMM registration to train deep learning algorithms capable of retrieving the localization of the tumor in the surgical position when a preoperative volume and a surgical surface are given as inputs. This method achieves an average tumor localization error of 15.46 ± 3.96 and an average surface projection distance of 13.38 ± 4.61. Given a preoperative volume and an intraoperative surface encoded in a distance field image, the method is able to generate a predicted displacement field in roughly 130 ms. Due to the high speed, this method could also be used in other real-time applications in surgery or radiation therapy. Furthermore, it could be used as an initial fast alignment before proceeding with other registration techniques. The network can easily generalize to other breast geometries that have not been seen during training, in contrast to other proposals that need new training for every new geometry (Mendizabal, Márquez-Neila, et al. 2020).

8.2 Contributions

The major contributions of our work are:

- Collection of a dataset with 67 clinical cases of preoperative breast MRI and supine CT images. This cohort represents the largest ever reported for prone to supine registration in the context of breast imaging, ensuring that different ages and sizes are represented.

- Development of a novel method for performing non-rigid landmark driven registration specifically designed to estimate the large deformation from breast prone to supine positions and to localize the tumor using only the intraoperative surface and the preoperative volume.

- First reported visco-hyperelastic characterization and modeling of the breast to simulate the patient-specific breast behavior under gravity loading, which provides a good estimation of tumor localization in the surgical position.

- Design and development of deep-learning based technique to align the volume extracted from a preoperative image and the intraoperative surface that is very computationally efficient and non-geometry specific.

In order to place the results and contributions of the work within the context of state of the art research, the following paragraphs provide a summary of the results of the proposed methodologies and of those of the state of the art studies. Table 8.1 summarizes the results of the proposed methodologies in terms of tumor distance and tumor skin-projection distance. Table 8.2 reports the results of alternative studies of the state of the art, including method used, dataset size, metric used for evaluation and registration error.

In can be noted that the first methodology *Landmark driven prone to supine non-rigid registration* described in Chapter 5 has been evaluated in a number of cases far greater than other proposals. Furthermore, the results have been obtained without biomechanical models or pixel intensity registration techniques and evaluated only in very few cases. This methodology has similar or better results when compared to other methods based only on biomechanical models and surface information (Eiben et al. 2016, Duraes et al. 2019). Moreover it is important to hightlight the methodological contribution to solve a large deformation registration problem robustly and requiring only the surface in the intraoperative position.

The second proposed methodology *Biomechanical modeling of the breast under gravity loading* described in Chapter 6 proposes a new biomechanical approach that describes the breast for the first time with a visco-hyperelastic constutive model and optimized based on the surface information and has been evaluated in 15 cases. The results obtained outperform other state of the art proposal of prone to supine registration that rely only on biomechanical models and surface information (Eiben et al. 2016, Duraes et al. 2019) and has comparable results to other methods that also involve further registration steps requiring changes in the clinical protocols (Han et al. 2013, Xue et al. 2021).

The third methodology *Learning the prone to supine breast deformation* presents a new surface-to-volume deep learning methdod that is geometry independent and improves significantly the computation time (130 ms). This method does not rely on biomechanical models and has been trained on displacement fields obtained with landmark driven non-rigid registration process. Preliminary results obtained in 10 cases have shown promising results.

Proposed Methodologies	Method	Dataset (evaluation)	Tumor / Skin-projection distances [mm]
Landmark driven prone to supine non-rigid registration	Landmark driven non-rigid registration	67	16.21 / 13.86
Biomechanical modeling of the breast under gravity loading	Biomechanical Model + Surface Information	15	9.68 / 7.66
Learning the prone to supine breast deformation	Deep-learning based Registration	10	15.46 / 13.38

Table 8.1: Overview of the proposed methodologies.

Work	Method	Dataset	Evaluation Metric	Registration Error
Carter et al. 2008	Biomechanical Model + Intensity-based Registration	2	Manually selected landmarks distance (8)	4.05 mm
Eiben et al. 2013	Biomechanical Model + Intensity-based Registration	1	Manually selected landmarks distance (14)	5.30 mm
Han et al. 2013	Biomechanical Model + Intensity-based Registration	5	Skin fiducials markers distance (9)	8.44 mm
Danch-Wierzchowska et al. 2016	Biomechanical Model	2	Tumor distance	20.00 mm
Eiben et al. 2016	Biomechanical Model + Surface Registration	3	Manually selected landmarks distance (9)	15.3 mm
Duraes et al. 2019	Biomechanical Model + Surface Information	9	Tumor skin-projection distance	20.8 mm
Xue et al. 2021	Biomechanical Model + Surface Information + Affine Registration	25	Tumor distance	8.05 mm

Table 8.2: Overview of methods proposed for prone to supine breast registration.

8.3 Future Work

Although the main idea of the thesis is to use the intraoperative surface of the patient acquired at the time of surgery, all developed techniques have been evaluated using prone MRI images and the skin outline from the supine CT image. Further research is guaranteed in a prospective study during surgery or biopsy using surface data acquired with an optical scanner. Preliminary experiments of this setup have confirmed the feasibility of acquisition and processing of the surface from the optical scan of the supine position, including the proper identification of the nipple from the texture map.

In the context of the biomechanical modeling of the breast, we have considered only gravity as the main force responsible for the deformation from the prone position to the supine position. However, since the breast model has been obtained from a preoperative MRI acquired under a gravity loading environment, the identification of the reference state (load-free state) could make the prediction of the final deformation more reliable. Additionally, we have considered full contact between the skin and the breast tissue; modeling the sliding between the skin and the breast could increase the accuracy of the model and make the surface data matching more reliable. The optimization procedure has been conducted offline. Further research will consider an online optimization of the patient-specific mechanical properties using only the surface data information. Furthermore, the results could be potentially improved using a further registration step (affine, non-rigid ICP, Bspline-based point registration, or landmark driven LDDMM) that would ensure better matching of the external surface. One important future application of this method will be to generate ground truth data for training deep learning algorithms. Multiple simulations of the same breast geometry under different loading conditions and varying material properties in the identified realistic ranges would allow to generate sufficient ground truth data to learn the underline mechanical model of the breast. Such model could be used for real-time application of deformation estimations during breast surgery.

In the context of learning the prone to supine deformation using deep learning techniques, the major limitation of our work was the limited amount of data. The previously mentioned use of the biomechanical model to generate simulated training data under different conditions could allow a more robust and mechanically plausible training scheme. Further collaboration with the Hospital Gregorio Marañon and other hospitals will additionally ensure the collection of new data. Furthermore, the training process is based on ground-truth DVFs that are generated using a landmark driven LDDMM with a very limited number of internal markers. Identifying more internal markers in addition to the tumor centroid could lead to a more realistic inference of internal displacement of the breast tissue and increase the reliability of the generated DVFs. In this line, the collaboration with the radiologists from the hospitals involved in our study is also essential.

Chapter 9 Publications

9.1 Journal articles

Alfano, F., Cordero-Grande, L., Ortuño, J.E., Ferreres García, K., García-Sevilla, M., Bueno Zamora, O., Herrero Conde, M., Lizarraga, S., Santos, A., Pascau, J., Ledesma-Carbayo, M.J. "Breast tumor localization by prone to supine landmark driven registration for surgical planning". IEEE Access, 10:122901-122911. Nov. 2022 (doi: 10.1109/ACCESS.2022.3223658).

Alfano, F., Bermejo-Pelaez, D., Cordero-Grande, J.E., Ferreres García, K., Bueno Zamora, O., Lizarraga, S., Santos, A., Pascau, J., Ledesma-Carbayo, M.J. "Learning Breast Tissue Behavior for Surgical Planning with Convolutional Neural Networks", to be submitted to Medical Image Analysis.

Alfano, F., Navas, P., Lamata, P., Ferreres García, K., Ortuño, J.E., Bueno Zamora, O., Lizarraga, S., Santos, A., Pascau, J., Goicolea, J.M., Ledesma Carbayo, M.J "Simulation of the Effect of Gravity for Breast Surgical Planning: Feasibility of a Visco-hyperelastic Mechanical Model", to be submitted to INTERFACE FOCUS.

9.2 Conference articles

Gorrin, N., **Alfano, F.**, Navas, P., Lamata, P., Ferreres García, K., Ortuño, J.E., Bueno Zamora, O., Lizarraga, S., Santos, A., Pascau, J., Goicolea, J.M., Ledesma Carbayo, M.J. "Biomechanical modelling of the behaviour of the human breast under the effect of gravity for tumor detection". Actas del XL Congreso Anual de la Soc. Esp. Ing. Biomédica, pág. 274-277. Valladolid. Nov. 2022.

Alfano, F., Ortuño Fisac, J.E., García-Sevilla, M., Herrero Conde, M., Bueno Zamora,

O., Lizarraga, S., Santos, A., Pascau, J., Ledesma-Carbayo, M.J. "Prone to Supine Surface Based Registration Workflow for Breast Tumor Localization in Surgical Planning". IEEE International Symposium on Biomedical Imaging (ISBI 2019), pp. 1150-1153. Venice (Italy), Apr. 2019. (doi: 10.1109/ISBI.2019.8759104).

Alfano, F., Pérez García, F., Ortuño Fisac, J.E., Herrero Conde, M., Bueno Zamora, O., Calvo, F.A., Lizarraga, S., Santos, A., Pascau, J., Ledesma-Carbayo, M.J. "Tumor localization using prone to supine surface based registration for breast cancer surgical planning". IEEE International Symposium on Biomedical Imaging (ISBI 2018), pp. 788-791. Washington D.C. (USA), Apr. 2018. (doi: 10.1109/ISBI.2018.8363690)

Alfano, F., Pérez García, F., Ortuño Fisac, J.E., Herrero Conde, M., Bueno Zamora, O., Calvo, F.A., Lizarraga, S., Santos, A., Pascau, J., Ledesma Carbayo, M.J. "Prone to supine surface-based registration for surgical planning in breast cancer treatment". Actas del XXXV Congreso Anual de la Soc. Esp. Ing. Biomédica, pág. 301-304. Bilbao. Nov/Dec. 2017.

Bibliography

Alderliesten, T. et al. (2013). "Deformable image registration by multi-objective optimization using a dual-dynamic transformation model to account for large anatomical differences". In: *Medical Imaging 2013: Image Processing*. Vol. 8669. SPIE, pp. 273–279.

Alfano, F. et al. (2019). "Prone to supine surface based registration workflow for breast tumor localization in surgical planning". In: *2019 IEEE 16th International Symposium on Biomedical Imaging (ISBI 2019)*. IEEE, pp. 1150–1153.

Audenaert, E. A. et al. (2019). "Cascaded statistical shape model based segmentation of the full lower limb in CT". In: *Computer methods in biomechanics and biomedical engineering* 22.6, pp. 644–657.

Avants, B. B. et al. (2008). "Symmetric diffeomorphic image registration with cross-correlation: evaluating automated labeling of elderly and neurodegenerative brain". In: *Medical image analysis* 12.1, pp. 26–41.

Azar, F. S. et al. (2001). "A deformable finite element model of the breast for predicting mechanical deformations under external perturbations". In: *Academic Radiology* 8.10, pp. 965–975.

Azoury, F. et al. (2009). "Thoracoscopic management of a pericardial migration of a breast biopsy localization wire". In: *The Annals of thoracic surgery* 87.6, pp. 1937–1939.

Babarenda Gamage, T. P. et al. (2019). "An automated computational biomechanics workflow for improving breast cancer diagnosis and treatment". In: *Interface Focus* 9.4, p. 20190034.

Balakrishnan, G. et al. (2018). "An Unsupervised Learning Model for Deformable Medical Image Registration". In: *2018 IEEE/CVF Conference on Computer Vision and Pattern Recognition*, pp. 9252–9260. arXiv: 1802.02604[cs].

— (2019). "VoxelMorph: A Learning Framework for Deformable Medical Image Registration". In: *IEEE Transactions on Medical Imaging* 38.8, pp. 1788–1800. arXiv: 1809.05231[cs].

Balkenende, L. et al. (2022). "Application of Deep Learning in Breast Cancer Imaging". In: *Seminars in Nuclear Medicine*. Elsevier.

Beg, M. F. et al. (2005). "Computing Large Deformation Metric Mappings via Geodesic Flows of Diffeomorphisms". In: *International Journal of Computer Vision* 61.2, pp. 139–157.

Boveiri, H. R. et al. (2020). "Medical image registration using deep neural networks: a comprehensive review". In: *Computers & Electrical Engineering* 87, p. 106767.

Cady, B. et al. (1996). "The new era in breast cancer. Invasion, size, and nodal involvement dramatically decreasing as a result of mammographic screening". In: *Archives of Surgery (Chicago, Ill.: 1960)* 131.3, pp. 301–308.

Calvo-Gallego, J. L. et al. (2018). "Comparison of different constitutive models to characterize the viscoelastic properties of human abdominal adipose tissue. A pilot study". In: *Journal of the mechanical behavior of biomedical materials* 80, pp. 293–302.

Cao, X. et al. (2018). "Deep learning based inter-modality image registration supervised by intra-modality similarity". In: *International workshop on machine learning in medical imaging*. Springer, pp. 55–63.

Carter, T. et al. (2008). "MR navigated breast surgery: method and initial clinical experience". In: *International Conference on Medical Image Computing and Computer-Assisted Intervention*. Springer, pp. 356–363.

Chadwick, D. R. et al. (1997). "Wire-directed localization biopsy of the breast: an audit of results and analysis of factors influencing therapeutic value in the treatment of breast cancer". In: *European Journal of Surgical Oncology: The Journal of the European Society of Surgical Oncology and the British Association of Surgical Oncology* 23.2, pp. 128–133.

Chan, B. K. et al. (2015). "Localization techniques for guided surgical excision of non-palpable breast lesions". In: *Cochrane Database of Systematic Reviews* 12.

Chung, J.-H. et al. (2008). "Modelling mammographic compression of the breast". In: *International conference on medical image computing and computer-assisted intervention*. Springer, pp. 758–765.

Conley, R. H. et al. (2015). "Realization of a biomechanical model-assisted image guidance system for breast cancer surgery using supine MRI". In: *International Journal of Computer Assisted Radiology and Surgery* 10.12, pp. 1985–1996.

Dalca, A. V. et al. (2018). "Unsupervised Learning for Fast Probabilistic Diffeomorphic Registration". In: vol. 11070, pp. 729–738. arXiv: 1805.04605[cs].

Danch-Wierzchowska, M., D. Borys, B. Bobek-Billewicz, et al. (2016). "Simplification of breast deformation modelling to support breast cancer treatment planning". In: *Biocybernetics and Biomedical Engineering* 36.4, pp. 531–536.

Danch-Wierzchowska, M., D. Borys, and A. Swierniak (2020). "FEM-based MRI deformation algorithm for breast deformation analysis". In: *Biocybernetics and Biomedical Engineering* 40.3, pp. 1304–1313.

Del Palomar, A. P. et al. (2008). "A finite element model to accurately predict real deformations of the breast". In: *Medical engineering & physics* 30.9, pp. 1089–1097.

Duraes, M. et al. (2019). "Surgery of nonpalpable breast cancer: First step to a virtual perioperative localization? First step to virtual breast cancer localization". In: *The Breast Journal* 25.5, pp. 874–879.

Ebrahimi, M. et al. (2014). "Using surface markers for MRI guided breast conserving surgery: a feasibility survey". In: *Physics in Medicine & Biology* 59.7, p. 1589.

Eiben, B. et al. (2013). "Biomechanically guided prone-to-supine image registration of breast MRI using an estimated reference state". In: *2013 IEEE 10th international symposium on biomedical imaging*. IEEE, pp. 214–217.

Eiben, B., V. Vavourakis, J. H. Hipwell, S. Kabus, T. Buelow, et al. (2016). "Symmetric biomechanically guided prone-to-supine breast image registration". In: *Annals of biomedical engineering* 44.1, pp. 154–173.

Eiben, B., V. Vavourakis, J. H. Hipwell, S. Kabus, C. Lorenz, et al. (2016). "Surface driven biomechanical breast image registration". In: *Medical Imaging 2016: Image-Guided Procedures, Robotic Interventions, and Modeling*. Vol. 9786. SPIE, pp. 282–291.

Fan, J. et al. (2019). "BIRNet: Brain image registration using dual-supervised fully convolutional networks". In: *Medical image analysis* 54, pp. 193–206.

Fang, Q. et al. (2009). "Tetrahedral mesh generation from volumetric binary and grayscale images". In: *2009 IEEE International Symposium on Biomedical Imaging: From Nano to Macro*. ISSN: 1945-8452, pp. 1142–1145.

Fourcade, C. et al. (2022). "Deformable image registration with deep network priors: a study on longitudinal PET images". In: *Physics in Medicine & Biology* 67.15, p. 155011.

Fu, Y. et al. (2020). "Deep learning in medical image registration: a review". In: *Physics in Medicine & Biology* 65.20, 20TR01.

Fung, Y.-c. (2013). *Biomechanics: mechanical properties of living tissues*. Springer Science & Business Media.

Gamage, T. P. B. et al. (2017). "Registration of Prone and Supine Breast MRI for Breast Cancer Treatment Planning". In: *Computational Biomechanics for Medicine*. Ed. by A. Wittek et al. Cham: Springer International Publishing, pp. 123–134.

Graham, S. J. et al. (1995). "Changes in fibroglandular volume and water content of breast tissue during the menstrual cycle observed by MR imaging at 1.5 t". In: *Journal of Magnetic Resonance Imaging* 5.6, pp. 695–701.

Han, L., J. H. Hipwell, B. Eiben, et al. (2013). "A nonlinear biomechanical model based registration method for aligning prone and supine MR breast images". In: *IEEE transactions on medical imaging* 33.3, pp. 682–694.

Han, L., J. H. Hipwell, C. Tanner, et al. (2011). "Development of patient-specific biomechanical models for predicting large breast deformation". In: *Physics in Medicine & Biology* 57.2, p. 455.

Han, L., J. A. Noble, et al. (2003). "A novel ultrasound indentation system for measuring biomechanical properties of in vivo soft tissue". In: *Ultrasound in medicine & biology* 29.6, pp. 813–823.

Hipwell, J. H. et al. (2007). "A new validation method for X-ray mammogram registration algorithms using a projection model of breast X-ray compression". In: *IEEE Transactions on Medical Imaging* 26.9, pp. 1190–1200.

Hopp, T., M. Dietzel, et al. (2013). "Automatic multimodal 2D/3D breast image registration using biomechanical FEM models and intensity-based optimization". In: *Medical Image Analysis* 17.2, pp. 209–218.

Hopp, T. and N. V. Ruiter (2012). "2D/3D registration for localization of mammographically depicted lesions in breast MRI". In: *International Workshop on Digital Mammography*. Springer, pp. 627–634.

Hu, X. et al. (2019). "Dual-Stream Pyramid Registration Network". In: p. 9.

Hwang, E. S. et al. (2013). "Survival after lumpectomy and mastectomy for early stage invasive breast cancer". In: *Cancer* 119.7, pp. 1402–1411.

Al-Ishaq, Z. et al. (2019). "Wire guided impalpable breast lesion localisation: old is gold?: Our experience and update on new techniques". English. In: *European Journal of Surgical Oncology* 45.2. Publisher: Elsevier, e102–e103.

Joshi, S. C. et al. (2000). "Landmark matching via large deformation diffeomorphisms". In: *IEEE transactions on image processing* 9.8, pp. 1357–1370.

Kikinis, R. et al. (2014). "3D Slicer: A Platform for Subject-Specific Image Analysis, Visualization, and Clinical Support". In: *Intraoperative Imaging and Image-Guided Therapy*. Ed. by F. A. Jolesz. New York, NY: Springer, pp. 277–289.

Kingma, D. P. et al. (2014). "Adam: A method for stochastic optimization". In: *arXiv preprint arXiv:1412.6980*.

Kiruparan, N. et al. (2021). "Use of wire guided localisation and radio-guided occult lesion localisation for non-palpable breast lesions: A systematic literature review and meta-analysis of current evidence". In: *Asian Journal of Surgery*.

Krouskop, T. A. et al. (1998). "Elastic moduli of breast and prostate tissues under compression". In: *Ultrasonic imaging* 20.4, pp. 260–274.

Kybic, J. et al. (2003). "Fast parametric elastic image registration". In: *IEEE Transactions on Image Processing* 12.11. Conference Name: IEEE Transactions on Image Processing, pp. 1427–1442.

Lago, M. A. et al. (2012). "Breast prone-to-supine deformation and registration using a Time-of-Flight camera". In: *2012 4th IEEE RAS EMBS International Conference on Biomedical Robotics and Biomechatronics (BioRob)*. ISSN: 2155-1782, pp. 1161–1163.

Lee, A. et al. (2010). "Breast Image Registration by Combining Finite Elements and Free-Form Deformations". In: *Digital Mammography*. Vol. 6136. Berlin, Heidelberg: Springer Berlin Heidelberg, pp. 736–743.

Lee, A. W. et al. (2013). "Breast lesion co-localisation between X-ray and MR images using finite element modelling". In: *Medical image analysis* 17.8, pp. 1256–1264.

Lee, M. K. et al. (2020). "A comparison of two non-radioactive alternatives to wire for the localization of non-palpable breast cancers". In: *Breast Cancer Research and Treatment* 182.2, pp. 299–303.

Mendizabal, A. (2020). "Machine Learning meets real-time Numerical Simulation - Application to surgical training, preoperative planning and surgical assistance". In: p. 167.

Mendizabal, A., P. Márquez-Neila, et al. (2020). "Simulation of hyperelastic materials in real-time using deep learning". In: *Medical Image Analysis* 59, p. 101569.

Mendizabal, A., E. Tagliabue, et al. (2020). "Physics-Based Deep Neural Network for Real-Time Lesion Tracking in Ultrasound-Guided Breast Biopsy". In: *Computational Biomechanics for Medicine*. Ed. by K. Miller et al. Cham: Springer International Publishing, pp. 33–45.

Mertzanidou, T., J. Hipwell, S. Johnsen, L. Han, B. Eiben, Z. Taylor, S. Ourselin, H. Huisman, R. Mann, U. Bick, et al. (2014a). "MRI to X-ray mammography intensity-based registration with simultaneous optimisation of pose and biomechanical transformation parameters". In: *Medical image analysis* 18.4, pp. 674–683.

Mertzanidou, T., J. Hipwell, S. Johnsen, L. Han, B. Eiben, Z. Taylor, S. Ourselin, H. Huisman, R. Mann, U. Bick, et al. (2014b). "MRI to X-ray mammography intensity-based registration with simultaneous optimisation of pose and biomechanical transformation parameters". In: *Medical Image Analysis* 18.4, pp. 674–683.

Mïra, A. et al. (2018). "A biomechanical breast model evaluated with respect to MRI data collected in three different positions". In: *Clinical Biomechanics (Bristol, Avon)* 60, pp. 191–199.

Onieva Onieva, J. et al. (2018). "Diffeomorphic lung registration using deep CNNs and reinforced learning". In: *Image Analysis for Moving Organ, Breast, and Thoracic Images*. Springer, pp. 284–294.

Ouyang, X. et al. (2020). "Preliminary feasibility study of imaging registration between supine and prone breast CT in breast cancer radiotherapy using residual recursive cascaded networks". In: *IEEE Access* 9, pp. 3315–3325.

Pallone, M. J. et al. (2014). "Supine Breast MRI and 3D Optical Scanning: A Novel Approach to Improve Tumor Localization for Breast Conserving Surgery". In: *Annals of Surgical Oncology* 21.7, pp. 2203–2208.

Palomar, A. P. del et al. (2008). "A finite element model to accurately predict real deformations of the breast". In: *Medical Engineering & Physics* 30.9, pp. 1089–1097.

Paszke, A. et al. (2019). "Pytorch: An imperative style, high-performance deep learning library". In: *Advances in neural information processing systems* 32.

Pfeiffer, M. et al. (2020). "Non-rigid volume to surface registration using a data-driven biomechanical model". In: *International Conference on Medical Image Computing and Computer-Assisted Intervention*. Springer, pp. 724–734.

Raith, S. et al. (2012). "Finite Element Simulation of the Deformation of the Female Breast Based on MRI Data and 3-D Surface Scanning: An In-Vivo Method to Assess Biomechanical Material Parameter Sets". In: *Proceedings of the 3rd International Conference on 3D Body Scanning Technologies, Lugano, Switzerland*, pp. 16–17.

Rajagopal, V. et al. (2008). "Creating Individual-specific Biomechanical Models of the Breast for Medical Image Analysis". In: *Academic Radiology* 15.11, pp. 1425–1436.

Richey, W. L. et al. (2021). "Impact of deformation on a supine-positioned image-guided breast surgery approach". In: *International Journal of Computer Assisted Radiology and Surgery* 16.11, pp. 2055–2066.

Rohé, M.-M. et al. (2017). "SVF-Net: Learning Deformable Image Registration Using Shape Matching". In: *Medical Image Computing and Computer Assisted Intervention - MICCAI 2017*. Ed. by M. Descoteaux et al. Vol. 10433. Series Title: Lecture Notes in Computer Science. Cham: Springer International Publishing, pp. 266–274.

Romrell, L. J. et al. (2009). "Anatomy of the breast, axilla, chest wall, and related metastatic sites". In: *Elsevier* The breast, pp. 21–38.

Ronneberger, O. et al. (2015). "U-net: Convolutional networks for biomedical image segmentation". In: *International Conference on Medical image computing and computer-assisted intervention*. Springer, pp. 234–241.

Rueckert, D. et al. (1999). "Nonrigid registration using free-form deformations: application to breast MR images". In: *IEEE Transactions on Medical Imaging* 18.8, pp. 712–721.

Ruiter, N., R. Stotzka, et al. (2006). "Model-based registration of X-ray mammograms and MR images of the female breast". In: *IEEE Transactions on Nuclear Science* 53.1. Conference Name: IEEE Transactions on Nuclear Science, pp. 204–211.

Ruiter, N., T. Müller, et al. (2004). *Registration of X-ray mammograms and MR-volumes of the female breast based on simulated mammographic deformation*. Mensch-und-Buch-Verlag.

Ruiter, N. V. et al. (2006). "Model-based registration of X-ray mammograms and MR images of the female breast". In: *IEEE Transactions on Nuclear Science* 53.1, pp. 204–211.

Samani, A. et al. (2001). "Biomechanical 3-D finite element modeling of the human breast using MRI data". In: *IEEE transactions on medical imaging* 20.4, pp. 271–279.

Schnabel, J. A. et al. (2003). "Validation of nonrigid image registration using finite-element methods: application to breast MR images". In: *IEEE transactions on medical imaging* 22.2, pp. 238–247.

Shimada, S. et al. (2019). "DispVoxNets: Non-Rigid Point Set Alignment with Supervised Learning Proxies". In: *2019 International Conference on 3D Vision (3DV)*. Québec City, QC, Canada: IEEE, pp. 27–36.

Skinner, K. A. et al. (2001). "Palpable Breast Cancers Are Inherently Different From Nonpalpable Breast Cancers". In: *Annals of Surgical Oncology* 8.9, pp. 705–710.

Smith, M. (2009). *ABAQUS/Standard User's Manual, Version 6.9*. English. United States: Dassault Systèmes Simulia Corp.

Sokooti, H. et al. (2019). "3D convolutional neural networks image registration based on efficient supervised learning from artificial deformations". In: *arXiv preprint arXiv:1908.10235*.

Solves-Llorens, J. A. et al. (2014). "A complete software application for automatic registration of x-ray mammography and magnetic resonance images". In: *Medical physics* 41.8Part1, p. 081903.

Sorkine, O. (2006). "Differential representations for mesh processing". In: *Computer Graphics Forum*. Vol. 25. 4. Wiley Online Library, pp. 789–807.

Sung, H. et al. (2021). "Global Cancer Statistics 2020: GLOBOCAN Estimates of Incidence and Mortality Worldwide for 36 Cancers in 185 Countries". In: *CA: A Cancer Journal for Clinicians* 71.3, pp. 209–249.

Susante, J. L. van et al. (1998). "Migration of the guide-wire into the pleural cavity after needle localization of breast lesions". In: *European Journal of Surgical Oncology: The Journal of the European Society of Surgical Oncology and the British Association of Surgical Oncology* 24.5, pp. 446–448.

Tanner, C., J. A. Schnabel, et al. (2006). "Factors influencing the accuracy of biomechanical breast models: Factors influencing the accuracy of biomechanical breast models". In: *Medical Physics* 33.6Part1, pp. 1758–1769.

Tanner, C., M. White, et al. (2011). "Large breast compressions: Observations and evaluation of simulations". In: *Medical physics* 38.2, pp. 682–690.

Taylor, Z. A. et al. (2009). "On modelling of anisotropic viscoelasticity for soft tissue simulation: numerical solution and GPU execution". In: *Medical Image Analysis* 13.2, pp. 234–244.

Tingen, J. S. et al. (2020). “Savi scout radar localization versus wire localization for breast biopsy regarding positive margin, complication, and reoperation rates”. In: *The American Surgeon* 86.8, pp. 1029–1031.

Vandeweyer, E. et al. (2002). “Quantification of glands and fat in breast tissue: an experimental determination”. In: *Annals of Anatomy = Anatomischer Anzeiger: Official Organ of the Anatomische Gesellschaft* 184.2, pp. 181–184.

Vavourakis, V. et al. (2016). “Multiscale mechano-biological finite element modelling of oncoplastic breast surgeryâ€”numerical study towards surgical planning and cosmetic outcome prediction”. In: *PloS one* 11.7, e0159766.

Veronesi, U. et al. (2002). “Twenty-year follow-up of a randomized study comparing breast-conserving surgery with radical mastectomy for early breast cancer”. In: *The New England Journal of Medicine* 347.16, pp. 1227–1232.

Volders, J. H. et al. (2016). “Current status of ultrasound-guided surgery in the treatment of breast cancer”. In: *World journal of clinical oncology* 7.1, p. 44.

Wang, X. et al. (2013). “A quantitative comparison of soft tissue compressive viscoelastic model accuracy”. In: *Journal of the mechanical behavior of biomedical materials* 20, pp. 126–136.

Wellman, P. S. (1999). *Tactile imaging*. Harvard University.

Wodzinski, M. et al. (2021). “Semi-supervised deep learning-based image registration method with volume penalty for real-time breast tumor bed localization”. In: *Sensors* 21.12, p. 4085.

Xiao, H. et al. (2020). “A review on 3D deformable image registration and its application in dose warping”. In: *Radiation Medicine and Protection* 1.04, pp. 171–178.

Xue, C. et al. (2021). “Multimodal Patient-specific registration for breast imaging using biomechanical modeling with reference to AI evaluation of breast tumor change”. In: *Life* 11.8, p. 747.

Yang, X. et al. (2017). “Quicksilver: Fast predictive image registration–a deep learning approach”. In: *NeuroImage* 158, pp. 378–396.